PHYSICAL REVIEW B **96**, 214206 (2017)

Resilience of hidden order to symmetry-preserving disorder

Marcello Calvanese Strinati,[1,2,3] Davide Rossini,[4] Rosario Fazio,[5,1] and Angelo Russomanno[1,5]
[1]*NEST, Scuola Normale Superiore and Istituto Nanoscienze-CNR, 56126 Pisa, Italy*
[2]*Département de Physique, Ecole Normale Supérieure / PSL Research University, CNRS, 24 rue Lhomond, 75005 Paris, France*
[3]*Department of Physics, Bar-Ilan University, 52900 Ramat-Gan, Israel*
[4]*Dipartimento di Fisica, Università di Pisa and INFN, Largo Pontecorvo 3, 56127 Pisa, Italy*
[5]*ICTP, Strada Costiera 11, 34151 Trieste, Italy*

(Received 30 August 2017; revised manuscript received 1 December 2017; published 20 December 2017)

We study the robustness of nonlocal string order in two paradigmatic disordered spin-chain models, a spin-1/2 cluster-Ising and a spin-1 XXZ Heisenberg chain. In the clean case, they both display a transition from antiferromagnetic to string order. Applying a disorder, which preserves the Hamiltonian symmetries, we find that the transition persists in both models. In the disordered cluster-Ising model, we can study the transition analytically—by applying the strongest coupling renormalization group —and numerically—by exploiting integrability to study the antiferromagnetic and string order parameters. We map the model into a quadratic fermion chain, where the transition appears as a change in the number of zero-energy edge modes. We also explore its zero-temperature-singularity behavior and find a transition from a nonsingular to a singular region, at a point that is different from the one separating nonlocal and local ordering. The disordered Heisenberg chain can be treated only numerically: by means of MPS-based simulations, we are able to locate the existence of a transition between antiferromagnetic and string-ordered phase, through the study of order parameters. Finally, we discuss possible connections of our findings with many-body localization.

DOI: 10.1103/PhysRevB.96.214206

I. INTRODUCTION

Since Landau, we know that phase transitions and symmetry breaking are strictly connected (see for instance Ref. [1]). Let us focus on zero-temperature quantum phase transitions (QPTs) [2]. In the ordered phase, there is a manifold of degenerate ground states, which have high entanglement and obey the same symmetries of the Hamiltonian. Nevertheless, any physical ground state breaks this symmetry: because of decoherence, the system always ends up in a superposition of these symmetry-preserving states, which has small entanglement and breaks the symmetry. This mechanism manifests in the expectation value Φ of some local operator $\hat{\Phi}(\mathbf{x})$ (the order parameter) being different from zero. Symmetry breaking always comes together with long-range order; in the thermodynamic limit, the order parameter in a ground state is infinite-range correlated, $\lim_{|\mathbf{x}-\mathbf{y}|\to\infty}\langle\hat{\Phi}^\dagger(\mathbf{x})\hat{\Phi}(\mathbf{y})\rangle_{\rm GS}=|\Phi|^2$. Although the value of Φ depends on the specific choice of the symmetry-breaking ground state, its modulus $|\Phi|^2$ is independent of it. Moreover, this correlator does not depend on the choice of the ground state, even if we consider a nonphysical symmetry-preserving ground state. From a physical point of view, the order parameter can be, for instance, the magnetization in the ferromagnetic transition (breaking of rotation symmetry) or the superconducting wave function in superconductivity (breaking of gauge symmetry).

This paradigm has been challenged in the last decades by the discovery of topological phase transitions, which are characterized by no local order parameter but by a global rearrangement of the system structure [3,4]. The landscape of topological phase transitions is extremely rich [5]; here, we specifically focus on a particular class of topological phases occurring in one-dimensional systems, for which the concept of hidden order has been put forward. In this case, the order parameter still exists, but it is a nonlocal one: it is a string operator involving the system in its globality. The most famous example of string order (SO) is in the Haldane phase of a spin-1 isotropic Heisenberg chain [6]. Let us focus on one-dimensional systems and call $\hat{\mathcal{O}}_{j,k}$ the SO parameter between two sites j and k: long-range order in the thermodynamic limit is given by $\lim_{|j-k|\to\infty}\langle\hat{\mathcal{O}}_{j,k}\rangle_{\rm GS}\neq 0$, where $\langle\cdot\rangle_{\rm GS}$ denotes the ground-state (GS) average. In this case, an infinite-range *nonlocal* correlator is different from zero and does not correspond to any local nonvanishing object. Examples of transitions to hidden SO phases are the one between a ferromagnet and the Haldane phase in spin-1 chains [7–9], and the one occurring in the extended Bose Hubbard model [10–12]. In some cases of hidden order, the nonlocal parameter has not yet been recognized or does not exist [13,14], and recently SO has been discovered in a periodically driven spin-1/2 chain [15].

Properties of systems undergoing QPTs are markedly altered by the presence of disorder. Disorder shifts the phase transition point and can also create new phases, like the Griffiths phase [16–19] in disordered ferromagnets, the insulating phase in disordered superconductors [20], the Bose-Glass phase in a disordered Bose-Hubbard model [21], and the many-body localized phase in short-range interacting quantum systems [22,23]. Very remarkable are the works by Dasgupta and Ma [24] and by Fisher [25], who are able to construct a renormalization group (RG) flow—the "strongest coupling renormalization group"—to understand phase transitions in such models. This RG method has been used afterwards for a large variety of random quantum and classical systems (see Ref. [26] for a review). Many works focused on disorder and phases with local order. The interplay of disorder and nonlocal SO has been considered in a comparatively small amount of papers. Reference [27] focused on disordered spin-1/2 ladders, which may describe the properties of spin-1

chains with SO [28]. The interest on the ladders was due to the fact that the application of strongest coupling RG to spin-1 chains is difficult due to the proliferation of large local spin terms. This difficulty has been overcome in Refs. [19,29,30]; in particular, Ref. [19] found a transition from a Griffiths to a disordered Haldane phase in an $S = 1$ disordered antiferromagnetic Heisenberg chain. The numerical demonstration of the persistence of the string order in this model (with a different disorder) and a detailed analysis of the zero-temperature-singularity behavior has been discussed in Ref. [30]. In these works, the form of the disorder has been chosen so to preserve the symmetries of the Hamiltonian. While for small disorder amplitudes the SO is preserved thanks to the topological protection, over a given threshold the nonlocal ordering is broken. The topological protection for small disorder is expected from general arguments, however, the breaking of SO for strong disorder and the properties of this transition are not trivial at all [30].

As far as we know, there are no studies on the effect of a strong disorder on the properties of a transition from a string nonlocal order to a local order (like ferro- or antiferro- magnetic). Here, we make a progress in this direction considering disordered spin-1 and spin-1/2 chains whose clean counterparts (the XXZ Heisenberg chain and the cluster-Ising model) are well known to display a transition from an antiferromagnetic (AF) to a string-ordered phase (the isotropic Heisenberg chain is the Haldane model). In the first case, we resort to numerics: using a variational algorithm based on the formalism of matrix-product states (MPS) [31], we find that a phase with SO actually does exist, even in the disordered model. We locate the phase transition point and observe that it is shifted by the disorder, with respect to the clean case. In the case of the disordered cluster-Ising model we can go further: by applying a strongest coupling RG transformation, we show the existence of an AF and a string-ordered phase, and analytically find the phase transition point. In this case, the model is solvable because it can be mapped to a disordered noninteracting fermion chain. In the fermionic representation, the transition is of topological nature and is characterized by the appearance of zero-energy edge modes. Finally, we study the zero-temperature-singularity behavior of the model, by numerically analyzing the properties of the logarithmic gap distribution and of the inverse average of the gap [19,30]. We find a transition between a nonsingular and a singular behavior when the disorder strength is increased. This transition point is different from the one between SO and AF: for our specific form of disorder, we see the existence of a nonsingular and a singular SO phase, similarly to the findings of Ref. [30]. Moreover, we observe that the AF phase is singular.

The paper is organized as follows. In Sec. II, we introduce the two models we are considering. In Sec. III, we study the AF/SO transition in the cluster-Ising chain. We do this both analytically (through the strongest coupling RG) and numerically (evaluating the appropriate correlators thanks to the free-fermion mapping); we also study the properties of edge modes in the fermionic representation. In Sec. IV, we study the AF/SO transition in the Heisenberg XXZ chain by resorting to MPS numerical simulations. Finally, in Sec. V, we draw our conclusions. In Appendix A, we show details on the strongest coupling RG transformation applied to the cluster-Ising chain, and in Appendix B, we discuss the appearance of kinks in the MPS approximation of the GS, which are due to a numerical artifact.

II. THE MODELS

In the following, we will consider two spin chains that exhibit a zero-temperature QPT between a Néel-like AF phase and a phase that is characterized by nonlocal SO. They are the spin-1/2 cluster-Ising model and the spin-1 XXZ Heisenberg chain. The two models enjoy a local $\mathbb{Z}_2$ and $\mathbb{D}_2$ symmetry, respectively. We thus expect the SO phase to exist also in the presence of disorder, as long as the local symmetry is not broken [32,33]. In this section, we introduce the two models by presenting their Hamiltonian together with some of their properties and the relevant antiferromagnetic and string order parameters.

A. Spin-1/2 cluster-Ising model

The simplest and exactly solvable model in this context is the so-called cluster-Ising model (CIM) [34,35], which is described by the Hamiltonian

$$\hat{H}_{\mathrm{CIM}} = \sum_j \big[- J_j \hat{\sigma}^x_{j-1} \hat{\sigma}^z_j \hat{\sigma}^x_{j+1} + \lambda_j \hat{\sigma}^y_j \hat{\sigma}^y_{j+1} \big]. \tag{1}$$

Here, $\hat{\sigma}^\alpha_j$ (with $\alpha = x,y,z$) denote the spin-1/2 Pauli matrices on the jth site of the chain ($j = 1, \ldots, L$, where L is the chain length), while J_j and λ_j denote the (possibly site-dependent) three-spin and two-spin coupling terms, respectively. In the following, we will always adopt open boundary conditions (OBC). After a standard Jordan-Wigner transformation [36] of the form $\hat{c}_j = (\prod_{m=1}^{j-1} \hat{\sigma}^z_m)\hat{\sigma}^-_j/2$, the Hamiltonian in Eq. (1) can be mapped onto a free-fermion model with nearest- and next-to-nearest-neighbor hopping terms

$$\hat{H}_{\mathrm{CIM}} = \sum_j [-J_j(\hat{c}^\dagger_{j-1} - \hat{c}_{j-1})(\hat{c}^\dagger_{j+1} + \hat{c}_{j+1}) + \lambda_j(\hat{c}^\dagger_j + \hat{c}_j)(\hat{c}^\dagger_{j+1} - \hat{c}_{j+1})], \tag{2}$$

in a way similar to the one-dimensional quantum Ising model in a transverse field [37]. This Hamiltonian is integrable, and its dynamics can be reduced to that of noninteracting fermionic quasiparticles: the GS is the BCS state without quasiparticles.

It has been proven [35] that, in the homogeneous case (i.e., $J_j = J$ and $\lambda_j = \lambda$ for all j), the system features a QPT between a conventional AF phase along the y direction and a phase with nonlocal SO (the so called "cluster phase"), when decreasing λ/J and crossing the critical value of 1.

The y antiferromagnet is detected by a local order parameter. In agreement with the discussion in the Introduction, we can express it as an infinite-range correlator:

$$\left(\mathcal{S}^y_{[1/2]}\right)^2 = \tfrac{1}{4} \lim_{l\to\infty} (-1)^l \left\langle \hat{\sigma}^y_k \hat{\sigma}^y_{k+l} \right\rangle. \tag{3}$$

To be precise, here, we are considering the square modulus of the order parameter, which is the same for all the degenerate symmetry-breaking ground states. Since this model breaks the $\mathbb{Z}_2$ symmetry (see below for more details), there are exactly two symmetry-breaking ground states, which differ for the sign

of the order parameter. Moreover, because we are evaluating the modulus of the order parameter as the limit of a correlator, it is not important to select the symmetry breaking ground states: the correlators are the same on all the states of the GS manifold. From a technical point of view, the mapping to the fermionic model is very important in order to evaluate this correlator. Thanks to Wick's theorem, it can be expressed as a Toeplitz determinant [38] of specific single-particle fermionic correlators of the Hamiltonian (2)—see Sec. III B for more details.

On the opposite, the cluster phase is characterized by a nonvanishing value of the nonlocal SO parameter, which is expressed as the infinite-range limit of a nonlocal correlator:

$$\mathcal{O}^z_{[1/2]} = \lim_{l\to\infty} (-1)^l \left\langle \hat\sigma^x_k \hat\sigma^y_{k+1} \left[\prod_{n=k+2}^{k+l-2} \hat\sigma^z_n\right] \hat\sigma^y_{k+l-1} \hat\sigma^x_{k+l} \right\rangle. \quad (4)$$

From a technical point of view, this nonlocal correlator is evaluated by applying to the Hamiltonian a duality transformation (see Ref. [35] and Appendix A for details). This nonlocal unitary transformation maps the Hamiltonian onto itself, with λ_j exchanged with J_j [see Eq. (A10)]. Moreover, the correlator of Eq. (4) is mapped on the AF correlator of Eq. (3), which can be evaluated as explained above.

Unless specified, here and in the following equations, we will omit the subscript $\langle \dots \rangle_{\rm GS}$ and consider all the expectation values on one of the degenerate ground states of the system. As remarked before, it is not important which GS in particular, the correlators being independent of the specific choice of the state in the GS manifold. Moreover, in the presence of disorder, we will average over many realizations: this operation will be denoted by an overline $\overline{\langle \dots \rangle}$. We notice that the disorder is not translationally invariant: translation invariance is restored after averaging over the disorder realizations. From a numerical point of view, we can only evaluate finite-range correlators: $\mathcal{O}^\alpha_{[1/2],l}$ (with $\alpha = x,y,z$) denotes the string correlator over a range l, such that $\mathcal{O}^\alpha_{[1/2]} = \lim_{l\to\infty} \mathcal{O}^\alpha_{[1/2],l}$. In a similar way, we define the finite-range AF correlator as $(\mathcal{S}^\alpha_{[1/2],l})^2$ such that $(\mathcal{S}^\alpha_{[1/2]})^2 = \lim_{l\to\infty} (\mathcal{S}^\alpha_{[1/2],l})^2$.

Let us now focus on the version of the Hamiltonian with disorder, which we are studying in the rest of the work. A necessary condition to preserve the string-ordered phase is the choice of a disorder that preserves the symmetry of the model: this is the symmetry broken by the GS in the phase transition. As mentioned above, the Hamiltonian in Eq. (1) enjoys a $\mathbb{Z}_2$ symmetry, since it is invariant under a rotation of angle π around the z axis: $\hat V^\dagger \hat H_{\rm CIM} \hat V = \hat H_{\rm CIM}$ with $\hat V = \exp(-i\frac{\pi}{2}\sum_j \hat\sigma^z_j)$. Being the symmetry group generated by only two operators ($\hat V$ and $\hat{\mathbb{I}}$), the GS manifold can have at most dimension two, so there can be at most two symmetry-breaking ground states. The invariance under the operator $\hat V$ implies

$$\left[\prod_j \hat\sigma^z_j, \hat H_{\rm CIM}\right] = 0. \quad (5)$$

A possibility to satisfy this condition in a disordered situation is to assume that both the site-dependent two-spin and the three-spin couplings are taken randomly from some probability distribution. In the following, we will specifically address the situation in which both the λ_j and the J_j are uniformly distributed over some interval $\lambda_j \in [0,\lambda_{\max}]$ and $J_j \in [0,J_{\max}]$, for all $j = 1,\dots,L$.

B. Spin-1 XXZ Heisenberg chain

The other model that we are going to focus on is a spin-1 XXZ Heisenberg chain, given by the Hamiltonian

$$\hat H_{\rm XXZ} = J \sum_j \left[\hat S^x_j \hat S^x_{j+1} + \hat S^y_j \hat S^y_{j+1} + \Lambda_j \hat S^z_j \hat S^z_{j+1}\right], \quad (6)$$

where $\hat S^\alpha_j$ (with $\alpha = x,y,z$) now denotes the spin-1 operators on the jth site, J is the energy scale of the nearest-neighbor spin coupling, and Λ_j is the anisotropy factor along the z axis, at site j. Contrary to the CIM, the spin-1 Heisenberg chain is a nonintegrable model and cannot be easily diagonalized. For this reason, numerical approaches based on exact diagonalization techniques or on MPS are usually employed in order to capture the GS physics. In the clean case, that is, for $\Lambda_j = \Lambda$, $\forall j$, model (6) is known to display a phase transition between a topological phase, usually referred to as the Haldane phase [6], and a nontopological Néel AF phase. Such transition has been studied in some details in the literature, and is expected to occur for $\Lambda \approx 1.186\dots$ [8,9].

In an open chain, the GS in the Haldane phase is identified by the presence of gapless spin-1/2 modes on top of a gapped bulk, which make the GS fourfold degenerate in the thermodynamic limit. This phenomenology is related to a hidden $\mathbb{D}_2$ symmetry breaking, described by the dihedral group of rotations [32,39]

$$\mathcal{G}_{\mathbb{D}_2} = \left\{\hat{\mathbb{I}}, e^{i\pi\sum_n \hat S^x_n}, e^{i\pi\sum_n \hat S^y_n}, e^{i\pi\sum_n \hat S^z_n}\right\}. \quad (7)$$

Because of the presence of such edge modes, a state in the Haldane phase is characterized by a hidden long-range order [40], which cannot be revealed by any expectation value of simple two-point correlators $\langle \hat S^\alpha_k \hat S^\alpha_{k+l}\rangle$. Indeed, their GS expectation values vanish in the limit $l\to\infty$. This hidden order can be seen by defining a nonlocal SO parameter for a spin-1 chain in a way similar to what has been done for the CIM (4):

$$\mathcal{O}^\alpha_{[1]} = \lim_{l\to\infty} \mathcal{O}^\alpha_{[1],l} = \lim_{l\to\infty} \left\langle \hat S^\alpha_k \left[\prod_{n=k+1}^{k+l-1} e^{i\pi \hat S^\alpha_n}\right] \hat S^\alpha_{k+l} \right\rangle, \quad (8)$$

such that the system is said to posses SO if the above limit is finite and nonvanishing. The presence of hidden order can be understood by remapping the model onto a ferromagnetic chain with four symmetry-broken states, by means of the Kennedy-Tasaki transformation [41]: string correlators are mapped onto two-point correlators, which indeed reveal the presence of ferromagnetic order. This is similar to what happens in the CIM, where a duality transformation maps the SO correlator of Eq. (4) onto the AF correlator of Eq. (3).

The physical meaning of the SO parameter (8) is very clearly expressed in Ref. [28]; we briefly review it here for reader's convenience: if we measure the value of the spin projections along α, we can find 1, 0, or -1, this being a spin-1 chain. Since the GS is a superposition of spin eigenstates, each time we measure, we find a different sequence of $+1$, 0, or -1, with some probability. The fact that the operator

(8) has a nonvanishing expectation value means that, if we withdraw the zeros from any of these sequences, we find alternatively $+1$ and -1: without the zeros, the system behaves antiferromagnetically. This property cannot be witnessed by any local operator: only the nonlocal string operator can do.

On the other hand, the presence of long-range AF order along the z axis in the Néel phase is witnessed by a nonzero value of the staggered two-point correlator

$$\left(\mathcal{S}^{\alpha}_{[1]}\right)^2 = \lim_{l\to\infty}\left(\mathcal{S}^{\alpha}_{[1],l}\right)^2 = \lim_{l\to\infty}(-1)^l\left\langle \hat{S}^{\alpha}_{k}\hat{S}^{\alpha}_{k+l}\right\rangle, \tag{9}$$

with $\alpha = z$ (this is the square value of the AF order parameter along α). Thus we can identify the Haldane phase of the XXZ chain by a nonzero SO [Eq. (8), for all α] and a vanishing expectation value of the staggered correlator in Eq. (9), for any α. Conversely, the Néel phase is identified by a vanishing SO $\mathcal{O}^{\alpha}_{[1]}$ for $\alpha = x, y$, and by a nonzero value of the staggered AF order parameter $\mathcal{S}^{z}_{[1]}$. We point out that we cannot use the SO along z as an order parameter of the Haldane phase because the observable $\mathcal{O}^{z}_{[1]}$ is nonzero both in the Haldane and in the Néel phases [42]. This can be simply understood in the large-Λ limit, where the GS is given by a product of consecutive states with opposite spin projection. From Eq. (8), it is clear that $\hat{\mathcal{O}}^{z}_{[1],l}$ evaluated on such GS is exactly -1 for all l, and in particular for $l \to \infty$.

We will model the disorder by taking Λ_j as a random variable, which is uniformly distributed between $\Lambda_{\min}$ and $\Lambda_{\max}$. We stress that a necessary condition for the GS to possess SO is to enjoy a unitary and local symmetry [33]. As stated before, since the presence of nonuniform anisotropy Λ_j does not break the $\mathbb{D}_2$ symmetry, the SO phase is expected to be present also in the disordered XXZ model, at least for some range of values $\Lambda_{\min}$ and $\Lambda_{\max}$ (see Appendix B 2 for an example of destruction of string order when a symmetry breaking term is added to the Hamiltonian).

III. ANTIFERROMAGNETIC-CLUSTER PHASE TRANSITION IN THE DISORDERED CIM

A. Strongest coupling RG approach

To understand whether the CIM can undergo a QPT or not, we perform a strongest coupling RG analysis in the thermodynamic limit $L \to \infty$, very similar in spirit to the one used in Ref. [25] for the disordered transverse field Ising model. We consider the largest value of the coupling

$$\Omega_I = \max\{J_j, \lambda_j\}. \tag{10}$$

The idea is to diagonalize the part of the Hamiltonian related to this coupling, assuming that it is so large that the corresponding term of the Hamiltonian can be considered as noninteracting, in a crudest approximation. The rest of the chain can be considered as a perturbation that changes the GS energy of this subsystem at second order in the coupling. At the end of the renormalization step, we take only the perturbed GS of the renormalized subsystem, and discard the rest of its local Hilbert space. In this way, at each renormalization step, we reduce the energy scale at which we are looking at the system: the considered site is renormalized away and an effective low-energy coupling term is generated. After many applications of the renormalization step, we asymptotically reach the GS and we can find its properties. One can distinguish between two possible cases, depending whether the largest coupling is a given J_j, or a given λ_j. We provide the derivation in full detail in Appendix A; here, we focus on its main points and their physical meaning.

We start assuming that the largest coupling is J_j: the part of the Hamiltonian corresponding to it is given by

$$\hat{H}_0 = -J_j\hat{\sigma}^{x}_{j-1}\hat{\sigma}^{z}_{j}\hat{\sigma}^{x}_{j+1}, \tag{11}$$

while the coupling to the rest of the system can be described by the following operator:

$$\hat{V} = \lambda_{j-1}\hat{\sigma}^{y}_{j-2}\hat{\sigma}^{y}_{j-1} + \lambda_{j+1}\hat{\sigma}^{y}_{j+1}\hat{\sigma}^{y}_{j+2}. \tag{12}$$

As detailed in Appendix A, it is possible to treat the term $\hat{V}$ perturbatively, applying a first-order perturbation theory to the four-fold degenerate GS of $\hat{H}_0$. After diagonalizing the resulting second-order perturbation matrix, we project over one of the perturbed ground states, ending up into eliminating site j and generating a new coupling:

$$-\widetilde{\lambda}_j\hat{\sigma}^{y}_{j-2}\hat{\sigma}^{y}_{j+2} \quad \text{with} \quad \widetilde{\lambda}_j \simeq \frac{\lambda_{j-1}\lambda_{j+1}}{J_j}. \tag{13}$$

The operators $\hat{\sigma}^{y}_{j-2/j+2}$ in Eq. (13) are in principle different from the unrenormalized ones: they coincide with them up to quartic terms in λ/J.

In the opposite case, where the largest coupling is λ_j, one can apply to Eq. (1) a duality transformation

$$\hat{\mu}^{x}_{j} = \prod_{k=1}^{j}\hat{\sigma}^{z}_{k}, \qquad \hat{\mu}^{z}_{j} = \hat{\sigma}^{x}_{j}\hat{\sigma}^{x}_{j+1}, \tag{14}$$

which maps the Pauli operators $\hat{\sigma}^{\alpha}_{j}$ onto different Pauli operators $\hat{\mu}^{\alpha}_{j}$. After the application of this transformation, the CIM Hamiltonian in terms of $\hat{\sigma}^{\alpha}_{j}$ [Eq. (1)] is re-expressed in terms of $\hat{\mu}^{\alpha}_{j}$ [see Eq. (A10) in Appendix A]: the transformed Hamiltonian has the same form of Eq. (1), but λ_j and J_j are now exchanged. The term with the largest coupling which has to be renormalized is now $\hat{\tilde{H}}_0 = -\lambda_j\hat{\mu}^{x}_{j-1}\hat{\mu}^{z}_{j}\hat{\mu}^{x}_{j+1}$. Applying to it the same analysis of the first case, we see that the renormalization procedure eliminates the site j in the dual representation, and generates the term

$$-\widetilde{J}_{j+1}\hat{\mu}^{y}_{j-2}\hat{\mu}^{y}_{j+2} \quad \text{with} \quad \widetilde{J}_j = \frac{J_{j-1}J_{j+1}}{\lambda_{j-1}}. \tag{15}$$

In the limit of many RG steps, and after applying the central limit theorem, it is possible to see that the disordered CIM is equivalent to a system with couplings

$$\begin{aligned}\widetilde{\lambda} &= \exp[2l(\overline{\ln\lambda} - \overline{\ln J})],\\ \widetilde{J} &= \exp[2l(\overline{\ln J} - \overline{\ln\lambda})],\end{aligned} \tag{16}$$

where l is the number of consecutive renormalized sites, which in principle can be different for different sites of the renormalized model (all the details of the calculation are in Appendix A). We can distinguish three cases.

I: $\overline{\ln\lambda} > \overline{\ln J}$. In this case, $\widetilde{\lambda}$ is larger than $\widetilde{J}$ exponentially in the number of iterations of the renormalization step. In the limit of infinite iterations, $\widetilde{J}$ is vanishingly small with respect to $\widetilde{\lambda}$: only the AF terms survive. Therefore the RG flows to an AF condition and the system is antiferromagnetic.

II: $\overline{\ln\lambda} < \overline{\ln J}$. Similarly to case I, in the limit of infinite iterations, $\widetilde{\lambda}$ is vanishingly small with respect to $\widetilde{J}$: only the three-body (cluster) terms survive. Looking at the problem in the dual representation, we see that the dual system has only the AF term and then the RG in this representation flows to an antiferromagnetic condition. Going back to the original representation, we see that the system flows to the SO phase.

III: $\overline{\ln\lambda} = \overline{\ln J}$. Here, the RG flows to a uniform system with $\widetilde{\lambda} = \widetilde{J} = 1$: the low-energy behavior of the model is equivalent to a uniform model at the critical point between the SO and the AF phase.

Therefore, also in the disordered model, we can predict a transition between AF and SO phase, occurring for

$$\overline{\ln\lambda} = \overline{\ln J}. \tag{17}$$

For $\overline{\ln\lambda} > \overline{\ln J}$, the model is AF, while for $\overline{\ln\lambda} < \overline{\ln J}$ it displays SO. These results are very similar to those found in the transverse field Ising model [25].

B. Numerical analysis of the two phases

Just to fix the ideas, let us now analyze the case in which there is no disorder on J ($J_j = 1, \forall j$), and each λ_j is taken from a uniform distribution among 0 and some $\lambda_{\max}$. In this case, the condition in Eq. (17) implies that the transition point is located at

$$\lambda^{(\infty)}_{\max,c} = \mathrm{e} \approx 2.718\ldots, \tag{18}$$

e being the Neper number. The superscript "(∞)" in Eq. (18) denotes that this is the critical point in the limit $L \to \infty$. By exploiting the fact that the CIM is exactly solvable, we can explore the behavior of the long-range string and AF correlator for considerably long system sizes, after averaging over an ensemble of several disorder realizations.

Here, we recall that, fixing the realization of the disorder, a Jordan-Wigner transformation is able to map Eq. (1) into a free-fermion diagonal form (irrespective of the presence or absence of translation invariance):

$$\hat{H} = \sum_{\mu=1}^{L} \epsilon_\mu (2\hat{\gamma}^\dagger_\mu \hat{\gamma}_\mu - 1), \tag{19}$$

where the single quasiparticle operators $\hat{\gamma}_\mu$ are defined in terms of the local fermionic operators $\hat{c}_j$ according to

$$\hat{\gamma}_\mu = \sum_{j=1}^{L} (U^*_{j\mu}\hat{c}_j + V^*_{j\mu}\hat{c}^\dagger_j), \tag{20}$$

and $U^*_{j\mu}$, $V^*_{j\mu}$ are the coefficients of the $2L \times 2L$ unitary matrix, which diagonalizes the appropriate $2L \times 2L$ Hermitian matrices forming the Hamiltonian (see, for instance, Ref. [43] for more details on this method). The GS is the one which is annihilated by all the $\hat{\gamma}_\mu$ operators (it has a BCS form). Thanks to this property, we can evaluate the AF correlator in Eq. (3). Applying Wick's theorem to the BCS Gaussian state, we can write the AF correlator as a Toeplitz determinant:

$$\left(\mathcal{S}^\alpha_{[1/2],l}\right)^2 = \frac{1}{4}\begin{vmatrix} G_{k,k+1} & \cdots & G_{k,k+l} \\ \vdots & & \vdots \\ G_{k+l-1,k+l} & \cdots & G_{k+l-1,k+l} \end{vmatrix}, \tag{21}$$

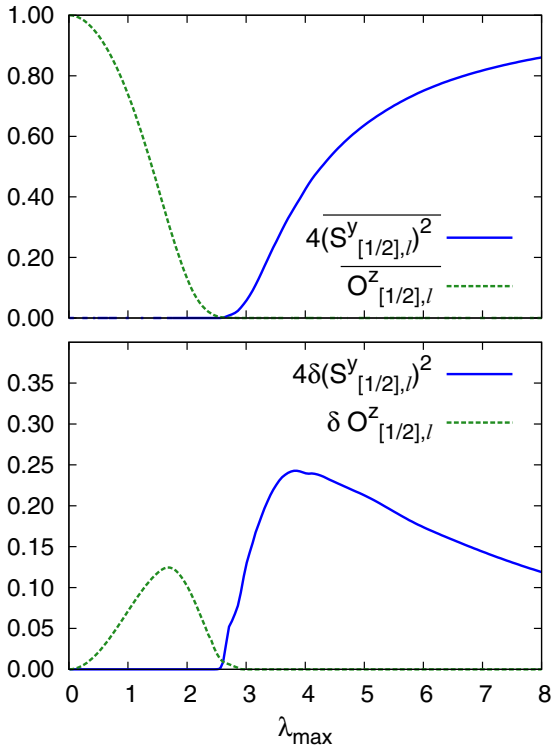

FIG. 1. (Top) AF (blue) and SO (green) parameters vs $\lambda_{\max}$ in the disordered CIM. The AF order has been approximated by the finite-range correlator $\overline{(\mathcal{S}^y_{[1/2],l})^2}$, while the SO by $\overline{\mathcal{O}^z_{[1/2],l}}$ (see Sec. II A). (Bottom) Fluctuations over the disorder of AF and SO correlators vs $\lambda_{\max}$ [see Eq. (24)]. We evaluated the correlators between site $l_0 = 60$ and site $L - 60$ (that is, $l = L - 120$). Data have been obtained for systems with $L = 500$ sites and after averaging over $N_{\mathrm{av}} = 200$ disorder realizations.

where, for each disorder realization, we have defined the two point fermionic correlators on the GS corresponding to that realization:

$$G_{j,m} = \langle(\hat{c}^\dagger_j - \hat{c}_j)(\hat{c}^\dagger_m + \hat{c}_m)\rangle. \tag{22}$$

Inverting Eq. (20) and using the fact that the GS is annihilated by all the $\hat{\gamma}_\mu$, we can evaluate this correlator as

$$G_{j,m} = \sum_\mu (V^*_{j\mu} - U_{j\mu})(U^*_{m\mu} + V_{m\mu}). \tag{23}$$

The SO parameter in Eq. (4) is evaluated by applying the duality transformation (14), which maps it onto an AF correlator of the form in Eq. (21), and the Hamiltonian onto another Hamiltonian of the same form. Finally, the results obtained through these formulas are averaged over N_{av} realizations of disorder.

The outcomes of our computations for a given finite size are reported in Fig. 1. On the upper panel, we plot $\overline{\mathcal{O}^z_{[1/2],l}}$ and $\overline{(\mathcal{S}^y_{[1/2],l})^2}$. In order to avoid unwanted boundary effects, we evaluate the correlators between sites that are far away from the chain ends (see the caption for details). These quantities approximate the order parameters of Eqs. (3) and (4), since in numerical simulations we can consider large, but yet finite system sizes. We see in the upper panel of Fig. 1 that, when

$\overline{\mathcal{O}^z_{[1/2],l}}$ vanishes, $\overline{(\mathcal{S}^y_{[1/2],l})^2}$ appears with a crossover: this is an indication that there is a transition from a string-ordered to a y-antiferromagnetic phase in the thermodynamic limit, even in the presence of disorder.

We can also analyze fluctuations over the disorder of the two order parameters. As before, we calculate finite-range correlators. Focusing on the AF order, we can define the fluctuation as

$$\delta\left(\mathcal{S}^y_{[1/2],l}\right)^2 = \left[\overline{\left\langle\hat{\sigma}^y_k\hat{\sigma}^y_{k+l}\right\rangle^2} - \overline{\left\langle\hat{\sigma}^y_k\hat{\sigma}^y_{k+l}\right\rangle}^2\right]^{1/2}, \qquad (24)$$

where the expectation value has to be intended over the GS of any specific disorder realization. The definition for the SO fluctuation ($\delta\mathcal{O}^z_{[1/2],l}$) is analogous, after replacing the correlator of Eq. (3) with that of Eq. (4). The results are shown in the lower panel of Fig. 1. We can see that the fluctuation is different from zero only when the corresponding order parameter is nonvanishing (compare with the upper panel): the finite-size crossover appears also in the behavior of fluctuations.

Until now, we have considered signatures of the transition in finite-length correlators. As we can observe in Fig. 1, finite-size effects are evident; for a given system size, we actually see a crossover, and there is a region where both the finite-range order parameters are different from zero. Moreover, if we identify the transition with the point where the curves of the two finite-range order parameters cross, we get a result that is different from the theoretical prediction (18). In order to properly infer the behavior in the thermodynamic limit $L,l \to \infty$, we perform a finite-size scaling analysis.

In order to reduce the effect of the fluctuations induced by the noise, we need to perform a coarse graininig in $1/l$ of disorder-averaged correlators. More precisely, we proceed in the following way. We fix the value of L and, in order to avoid finite-size boundary effects, we fix an appropriate l_0 and consider the disorder-averaged correlator between the site l_0 and the site $l_0 + l$, with l varying between 0 and $L - 2l_0$. Then, we coarse grain this correlator: we consider the interval in which the quantity $1/l$ varies, divide this interval in windows of width $\delta(1/l)$ and perform the average of the correlator over each window. For each of the resulting values, we evaluate the uncertainty as the maximum over the corresponding window of the disorder fluctuation of the correlator: applying the central limit theorem, this fluctuation is given by the value in Eq. (24) divided by $\sqrt{N_{\rm av}}$. We label each of the windows over which we coarse grain with its central value $1/l$; for each value of $1/l$, we locate the approximate transition point as the value of $\lambda_{\rm max}$ where the two coarse-grained correlators cross; we denote the crossing point as $\lambda^{(l)}_{{\rm max},c}$. In the upper panel of Fig. 2, we show $\lambda^{(l)}_{{\rm max},c}$ versus $1/l$: taking into account the error bars, we see a behavior consistent with a convergence towards the theoretical value of Eq. (18) when $1/l \to 0$. The error bars are evaluated in the following way: each time we add or subtract the uncertainties discussed above to the coarse-grained disorder-averaged correlators and then we take the half-dispersion of the four resulting estimates of the crossing.

The lower panel of Fig. 2 shows that the height $w^{(l)}$ of the crossing point tends to zero when $1/l \to 0$ (the error bars are evaluated with the same method used for $\lambda^{(l)}_{{\rm max},c}$). We have

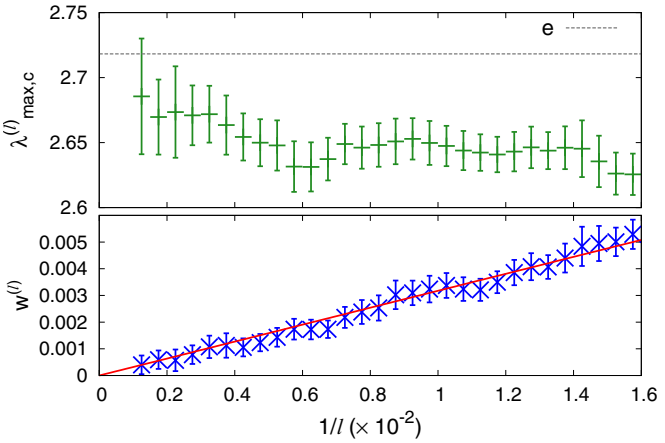

FIG. 2. (Top) Location of the finite-size crossing point $\lambda^{(l)}_{{\rm max},c}$ between AF and SO parameters vs $1/l$; for $1/l \to 0$, the crossing point tends to the theoretical transition value of Eq. (18), consistently with the error bars resulting from disorder-averaging+coarse-graining fluctuations (see the main text). (Bottom) The height $w^{(l)}$ of the crossing point vanishes for $1/l \to 0$ as confirmed by the straight-line fit (red line—see the main text). (Numerical parameters: $l_0 = 60$, $N_{\rm av} = 1000$, $\delta(1/l) = 5 \times 10^{-4}$, and $L = 1100$.)

checked this fact by fitting with a straight line $a \cdot (1/l)$, and found $(a = 317 \pm 4) \times 10^{-5}$ (red line in Fig. 2). This means that, in the thermodynamic limit, $w^{(\infty)} = 0$, and thus there is no region where both the order parameters are nonvanishing: when one vanishes the other appears, as appropriate for a QPT.

C. Edge modes

For a clean system, the QPT in the spin chain maps to a topological transition in the fermionic representation. In the case of periodic boundary conditions, the AF phase corresponds to winding number one in the fermionic picture, while the SO phase corresponds to winding number two [35,44]. Taking OBC, the topological nature of the system appears through the existence of zero-energy boundary modes [46,47]: diagonalizing the fermionic Hamiltonian, some vanishing ϵ_μ appear in Eq. (19). For each phase, there is a fixed number of zero-energy modes, and their amplitudes U_j and V_j [see Eq. (20)] are localized on the edges of the system. The AF phase displays one zero-energy mode, while the SO phase has two zero-energy modes (edge modes in uniform fermionic Hamiltonians very similar to Eq. (2) have been studied in Refs. [48,49]).

Even in the presence of disorder, we numerically observe the persistence in the spectrum of zero-energy modes (two modes in the SO phase, and one mode in the AF phase). Two examples of this fact are reported in Fig. 3. Here, we choose a specific disorder realization and show the single quasiparticle spectrum ϵ_μ for a case where the system shows SO ($\lambda_{\rm max} = 0.8$) and a case where it is AF ($\lambda_{\rm max} = 4.8$). In the first situation, there are two levels with energy many orders of magnitude smaller than the others; in the second one, there is a single level with this property: these levels correspond to the boundary modes discussed above (the energy is not exactly zero, due to the numerical round-off errors). We have verified that the same structure of the spectrum appears for any disorder realization.

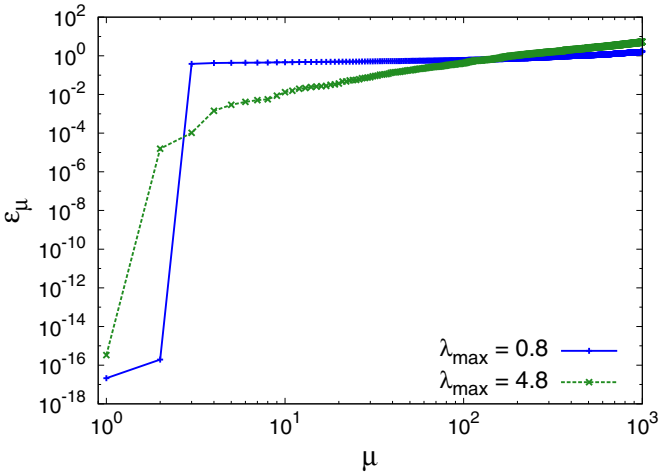

FIG. 3. Single quasiparticle energy eigenvalues ϵ_μ in increasing order for two values of λ_{max}. For $\lambda_{max} = 0.8$, the system is in the SO phase and displays two zero-energy boundary modes (they appear as two energy eigenvalues with energy many orders of magnitude smaller than the others). For $\lambda_{max} = 4.8$, the system is in the AF phase and shows one boundary mode. Here we considered $L = 1000$ and took one single realization of disorder.

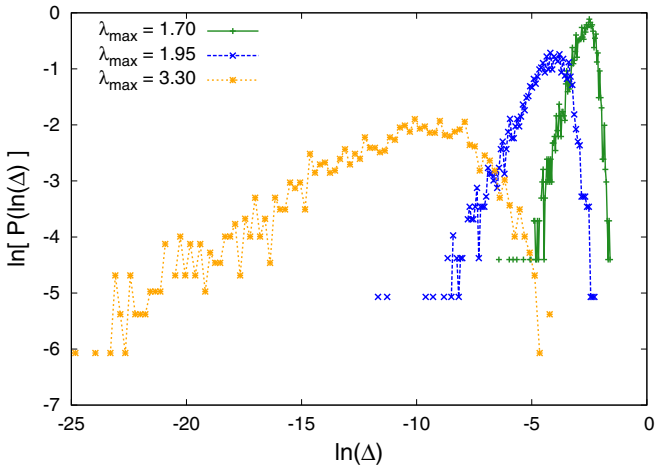

FIG. 4. Logarithmic level spacing distributions: in the bilogarithmic plots the power law at small Δ appears as a linear behavior. We use periodic boundary conditions in order to avoid the boundary zero-energy modes. (Numerical parameters: $N_{av} = 2000$ and $L = 400$.)

These edge modes are topologically protected, since they only depend on global properties of the system: they cannot be destroyed by local perturbations (like disorder) if the perturbation is weak enough. That is why, if we add disorder, two edge modes and the associated SO persists for λ_{max} small, and one edge modes and AF order persist for λ_{max} large. For λ_{max} around the transition, the disorder is strong enough to move the transition point.

D. Thermodynamic singularities

Disordered systems can display phases where the thermodynamic quantities show singularities in the limit of vanishing temperature [16,19,30]. This can be seen from the behavior of the distribution of the energy gap Δ of the Hamiltonian. If for small Δ the logarithmic energy gap distribution behaves as $P(\ln \Delta) \sim \Delta^{1/z}$ (z is the so-called dynamic exponent), it is easy to show that the excitation energy over the ground state behaves as $E_{ex}(T) \sim T^{1+1/z}$ at low temperatures. Therefore the low-temperature specific heat behaves as $C \sim T^{1/z}$ and its derivative shows a divergence in the limit of $T \to 0$ when $z > 1$. The ranges of parameters where this happens are called singular regions [30]; in order to find them, we numerically consider the properties of $P(\ln \Delta)$ and we check that it behaves as a power law for small Δ (see some examples in Fig. 4).

Applying a linear fit to the plots of $\ln[P(\ln \Delta)]$ vs $\ln \Delta$ we are able to estimate the value of the dynamic exponent z which we plot in Fig. 5. We see that there is a singular region with $z > 1$ for λ_{max} above a threshold $\lambda^{cs}_{max} \simeq 2$. In order to have a better estimate of λ^{cs}_{max}, we follow Ref. [30] and consider the behavior of the inverse average of the gap defined as

$$\Delta^{iv} \equiv \left[\overline{\left(\frac{1}{\Delta}\right)}\right]^{-1}, \tag{25}$$

where the average is performed over the disorder distribution. This object vanishes whenever the system is in a singular region [30] with $z > 1$; we show results for our case in Fig. 6. We see that Δ^{iv} vanishes for $\lambda_{max} > \lambda^{cs}_{max} = 2$, confirming that in this parameter range our system is singular. Moreover, we can numerically find that Δ^{iv} vanishes as a power law when λ approaches the transition point λ^{cs}_{max} from below: we have $\Delta^{iv} \sim (\lambda^{cs}_{max} - \lambda_{max})^{\mu_\Delta}$ with $\mu_\Delta = 2.06 \pm 0.01$.

In conclusion, we see a transition to a singular regime, which occurs at a critical value λ^{cs}_{max} different from the critical point $\lambda_{max,c}$ separating the SO and the AF phase. While for $\lambda_{max} > \lambda_{max,c}$ the system is AF and singular, we have a nonsingular SO phase ($z < 1$) for $\lambda_{max} < \lambda^{cs}_{max}$ and there is a singular SO phase ($z > 1$) for $\lambda^{cs}_{max} < \lambda_{max} < \lambda_{max,c}$. This behavior is strictly reminiscent of the disordered $S = 1$ antiferromagnetic Heisenberg chain [30] where there is a

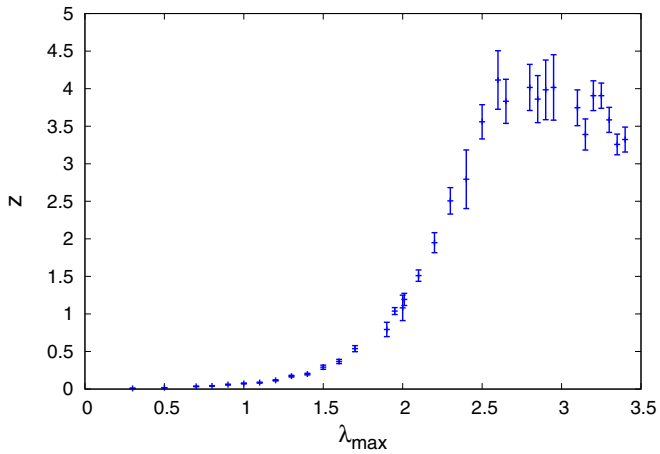

FIG. 5. Plot of the dynamic exponent z obtained from the fit of the logarithmic level spacing distribution $P(\ln \Delta)$ vs λ_{max}. For λ_{max} above a threshold $\lambda^{cs}_{max} \simeq 2$, it becomes larger than 1 giving rise to a singular behavior. (Numerical parameters: $N_{av} = 2000$, $L = 400$, periodic boundary conditions.)

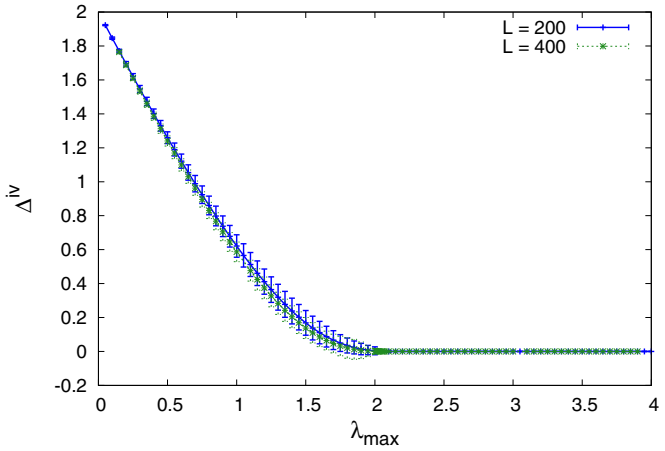

FIG. 6. Plot of the inverse average of the gap vs λ_{max}. It vanishes for $\lambda_{max} > \lambda^{cs}_{max} = 2$: this parameter range corresponds to a singular region ($z > 1$). (Numerical parameters: $N_{av} = 2000$ and periodic boundary conditions.)

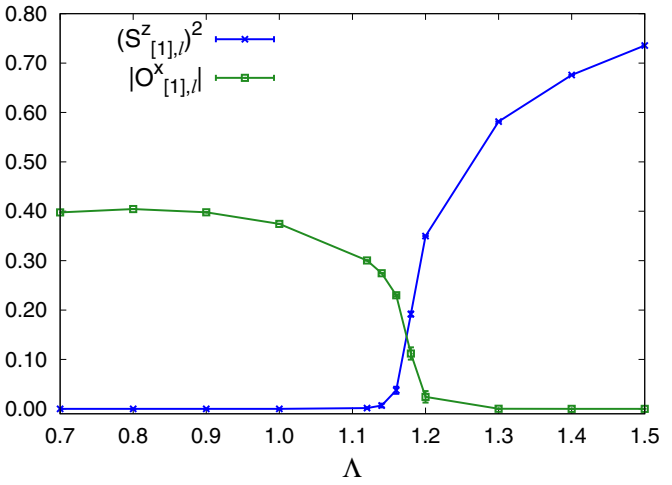

FIG. 7. The AF (blue) and SO (green) parameters for the clean XXZ model ($\Lambda_j = \Lambda$, $\forall j$), as a function of the anisotropy Λ. As we did for the CIM, the AF order has been approximated by the finite-size correlator $(\mathcal{S}^z_{[1],l})^2$, while the SO by $|\mathcal{O}^x_{[1],l}|$ (see Sec. II B). Here we simulated a chain of $L = 240$ sites and evaluated the correlators between site $k = 24$ and site $k + l = 120$ (that is $l = 96$), as also explained in Fig. 1 for the CIM. We locate the transition point at the crossing of the two curves, that is, $\Lambda^{(L)}_c = 1.17 \pm 0.01$. We estimate the uncertainty over $\Lambda^{(L)}_c$ as half of the discretization of Λ in proximity of the crossing point.

gapped Haldane phase ($z < 1$) and a singular Haldane phase ($z > 1$), both showing SO. We emphasize that the singularity structure of the phases is strictly related to the specific form of the disorder: for instance, taking λ uniform and J_j uniformly distributed between 0 and some J_{max}, we would have seen a nonsingular AF phase together with a singular AF phase, while the SO phase would have been fully nonsingular.

IV. HALDANE TO NÉEL PHASE TRANSITION IN THE DISORDERED SPIN-1 XXZ MODEL

We now switch to study the zero-temperature properties of the disordered spin-1 XXZ Hamiltonian of Eq. (6). Since this model is nonintegrable, in order to find the GS of a given finite-size system, we resort to a variational search on the class of MPS [31]. In our simulations, we analyze chains of up to $L = 240$ sites and choose a maximum bond link $D_{max} = 400$. We set J as the reference energy scale, and consider $J = 1$ in the following. As we have done in the CIM, to characterize the two phases, we focus on the finite-system AF correlation function $(\mathcal{S}^z_{[1],l})^2$ and on the x-axis string operator $\mathcal{O}^x_{[1],l}$ [the corresponding order parameters are defined, in the thermodynamic limit, by Eqs. (8) and (9)]. Since we have $(\mathcal{S}^z_{[1],l})^2 \geqslant 0$ and $\mathcal{O}^x_{[1],l} \leqslant 0$ in the XXZ chain, in the following, we will consider the absolute value of the string parameter in order to deal with positive quantities.

Before analyzing in detail the phase transition in the presence of disorder, let us briefly discuss the clean XXZ model. The situation is summarized in Fig. 7, which shows the behavior of the bulk expectation value of the staggered correlator along z (blue data set), and of the absolute value of the string correlator along x (green data set). We see that, at a critical value $\Lambda^{(L)}_c$ of the anisotropy term, the SO vanishes and the staggered order starts to take a finite value: as explained before, this is an indication of the occurrence of the Haldane-Néel phase transition. The position of the critical point in the thermodynamic limit, $\Lambda^{(\infty)}_c$, can be inferred from the finite-size scaling of the crossing point between the two curves; from our simulations at finite L, we estimate $\Lambda^{(L)}_c = 1.17 \pm 0.01$, which is in agreement with the value $\Lambda^{(\infty)}_c \simeq 1.186\ldots$ found in the thermodynamic limit [8,9].

Based on our knowledge on the clean XXZ model, we now focus on the Haldane-Néel phase transition in the disordered scenario. Since MPS simulations are computationally more demanding and can only afford systems with a comparatively small length, we adopted a procedure slightly different from the one used for the CIM, in order to estimate the SO correlator [Eq. (8)] and the AF correlator [Eq. (9)] from the bulk expectation values of the corresponding finite-size correlators. The two methods coincide in the thermodynamic limit, but the one described here is more appropriate for the smaller values of system size and number of disorder realizations which we can obtain with DMRG in the XXZ chain, because it enables to minimize the uncertainty in the averages.

Namely, we are interested in computing the bulk expectation values of a given two-point observable, of the form $\hat{\mathcal{A}}_{k,k+l}$. We recall that both the AF correlator, $(\mathcal{S}^\alpha_{[1],l})^2$, and the SO correlator, $\mathcal{O}^\alpha_{[1],l}$, can be seen as expectation values of observables which live on a given number of sites in between the kth and the $(k + l)$th site. After fixing the system size and the disorder realization, we first compute a space average over different lengths l of the correlator [50], in order to average out space fluctuations. We discard the sites that are close to the two chain ends, thus disregarding boundary effects (see Appendix B for details). Then, we repeat the simulation by varying the configuration of the disorder, and eventually perform a second average of such obtained space averages, over different disorder realizations. The obtained correlators have an uncertainty (denoted by error bars in Fig. 8), which is estimated by computing the variance of the space averaged

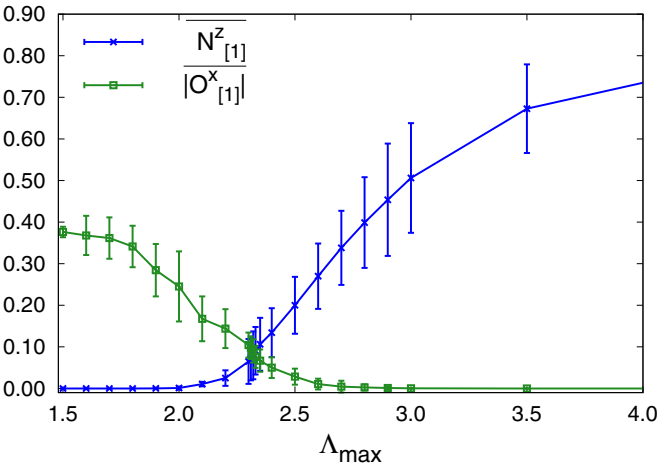

FIG. 8. AF (blue) and SO (green points) correlators averaged over space and over $N_{av} = 40$ realizations of disorder [Eqs. (B1) and (B2)], as a function of Λ_{max}. The error bars are computed as the square root of the variance over disorder [Eq. (B4)]. Here, we use $L = 120$, $\Lambda_{min} = 0$, and locate the transition at the intersection of the two curves: $\Lambda^{(L)}_{max,c} = 2.32 \pm 0.01$.

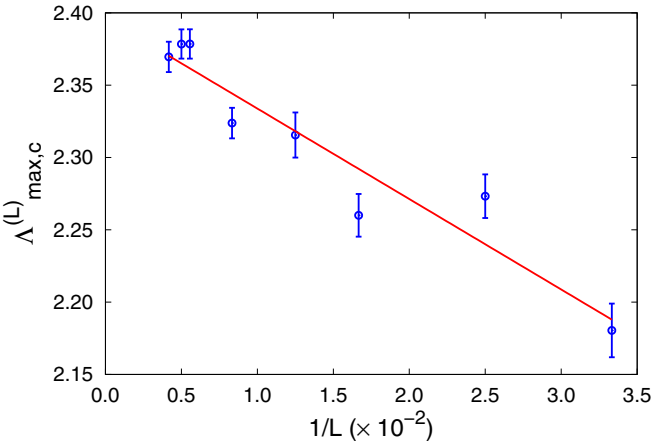

FIG. 9. Finite-size scaling for the critical point $\Lambda^{(L)}_{max,c}$ with $\Lambda_{min} = 0$. The data are shown as a function of $1/L$. Blue points correspond to the numerical data of $\Lambda^{(L)}_{max,c}$, (the uncertainty is estimated as in Fig. 7). The red solid line is the fit with the function $f(L) = a/L + \Lambda^{(\infty)}_{max,c}$, treating a and $\Lambda^{(\infty)}_{max,c}$ as fit parameters. Here, $\Lambda^{(\infty)}_{max,c}$ is the critical point in the thermodynamic limit, which we estimate as $\Lambda^{(\infty)}_{max,c} = 2.40 \pm 0.01$.

correlators for the different realizations of disorder, as detailed in Appendix B.

We first present our numerical analysis for Λ_j uniformly distributed in the interval $[0, \Lambda_{max}]$, for all j. In this case, we expect the system to undergo the Haldane-Néel phase transition as Λ_{max} is varied across some critical value. In our simulations we see that, in the Néel phase, the AF pattern is affected by the presence of kinks (domain walls, where the AF pattern is reversed), which hide the presence of long-range AF order (9). As detailed in Appendix B, the presence of such kinks is a numerical artifact due to the nonperfect convergence of the MPS algorithm. Thus, instead of computing the staggered correlator as in Eq. (9), we can get rid of the kinks and reveal the presence of AF long-range order by computing the bulk average [Eq. (B1)] of the Néel correlator, which is defined as

$$\mathcal{N}^z_{[1],l} = \left|\langle \hat{S}^z_k \hat{S}^z_{k+l} \rangle\right|. \tag{26}$$

Notice that $(\mathcal{S}^z_{[1],l})^2$ coincides with the Néel correlator in Eq. (26) in the case of perfect AF order (no kinks), but differently from the staggered correlator, $\mathcal{N}^z_{[1],l}$ is insensitive to such numerical artifacts, because of the presence of the absolute value in Eq. (26). Thus we characterize Haldane and Néel phases in the disordered chain by looking respectively at the SO along x [see Eq. (8)] and the Néel correlator in the limit of $l \to \infty$: $\mathcal{N}^z_{[1]} = \lim_{l\to\infty} \mathcal{N}^z_{[1],l}$.

In Fig. 8, we show the result of simulations with $L = 120$ and $\Lambda_{min} = 0$, after averaging over space and over disorder. Blue points correspond to the Néel order, $\overline{\mathcal{N}^z_{[1]}}$, whereas green points are the SO data, $\overline{|\mathcal{O}^x_{[1]}|}$. We observe that the Néel order is zero for sufficiently small Λ_{max}, and starts to increase around a given value of Λ_{max}. Conversely, the SO along x is nonzero for small Λ_{max}, and goes to zero as Λ_{max} is increased. This behavior is analogous to the one for the Haldane-Néel phase transition in the clean XXZ model (Fig. 7). Furthermore, we can estimate a critical point $\Lambda^{(L)}_{max,c}$, which is shifted with respect to the clean value: for the simulation in Fig. 8, we find $\Lambda^{(L)}_{max,c} = 2.32 \pm 0.02$. For a given finite size, the transition behaves as a crossover, exactly as it occurs for the CIM (upper panel of Fig. 1), and we estimate the finite-L approximation of the critical point as the abscissa of the crossing point of the two curves of the correlators. The error bars of the crossing points are estimated as follows. We consider the plot of the correlators (for instance Fig. 8) and, being interested in the fluctuations of the intersection of the disorder averages, we divide the error bars by $\sqrt{N_{av}}$, according to the central limit theorem. Later, we proceed in a way similar to Fig. 2: each time we add or subtract these fluctuations to the disorder-averaged correlators and then we take the half-dispersion of the four resulting values of the crossing. This gives the uncertainty of the crossing point.

As in the CIM case, in order to extrapolate the value of the critical point in the thermodynamic limit, we need to perform a finite-size scaling analysis and repeat the same simulations as in Fig. 8 for different values of L. The result is shown in Fig. 9: blue points correspond to the estimated values of $\Lambda^{(L)}_{max,c}$, and uncertainties are computed as explained above. To find the thermodynamic value of the critical point, we show the data as a function of $1/L$ and perform a best fit with the function $f(L) = a/L + \Lambda^{(\infty)}_{max,c}$. From the result in Fig. 9, we extrapolate the critical value in the asymptotic $L \to \infty$ limit: $\Lambda^{(\infty)}_{max,c} = 2.40 \pm 0.01$.

We can also define the height of the crossing point $w^{(L)}$, as in Sec. III B. For each value of L, the uncertainty on the value of $w^{(L)}$ is computed from that of the disorder-averaged correlators. We show the result in Fig. 10, from which we see that $w^{(L)}$ decreases as L is increased. From the fit, we estimate $w^{(\infty)} = 0.06 \pm 0.01$. This is an indication of the fact that the phase transition becomes sharper and sharper as L is increased.

So far, we have discussed the Haldane-Néel phase transition for Λ_j uniformly distributed in the interval $[\Lambda_{min}, \Lambda_{max}]$, for

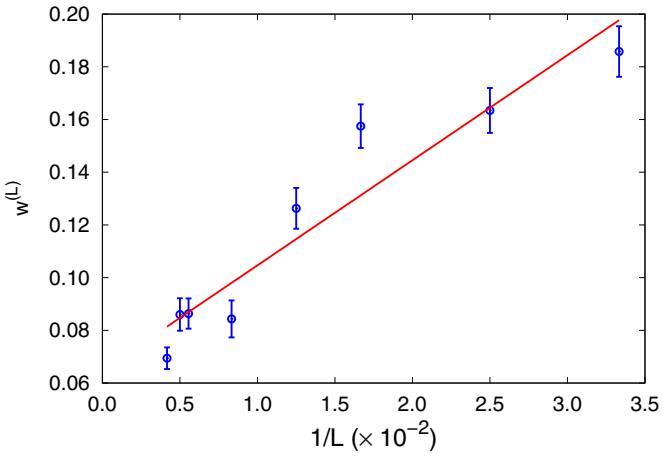

FIG. 10. Finite-size scaling for the height of the crossing point $w^{(L)}$ with $\Lambda_{\min} = 0$. Data (symbols) are shown as a function of $1/L$, and their uncertainties are computed from those of the disorder-averaged correlators. We see that the height of the crossing point decreases in the thermodynamic limit, meaning that the transition becomes sharper and sharper as L is increased.

all j, using $\Lambda_{\min} = 0$. In order to see how the position of the critical point is affected by the choice of $\Lambda_{\min}$ and $\Lambda_{\max}$, we simulate the disordered model of Eq. (6) varying $\Lambda_{\max}$ and using $\Lambda_{\min} = \Lambda_{\max}/(n+1)$, where n is a positive integer number. Our results for $L = 120$ are shown in Fig. 11. For each value of n, we estimate the position of the critical point $\Lambda^{(L)}_{\max,c}(n)$ as explained for the data in Fig. 7. If we define the algebraic average of $\{\Lambda_j\}$ in the chain, i.e.,

$$\bar{\Lambda} = \frac{\Lambda_{\min} + \Lambda_{\max}}{2} = \frac{\Lambda_{\max}}{2}\,\frac{n+2}{n+1}, \tag{27}$$

we find that the Haldane-Néel phase transition in the disordered chain occurs when $\Lambda_{\max}$ is such that the mean value of

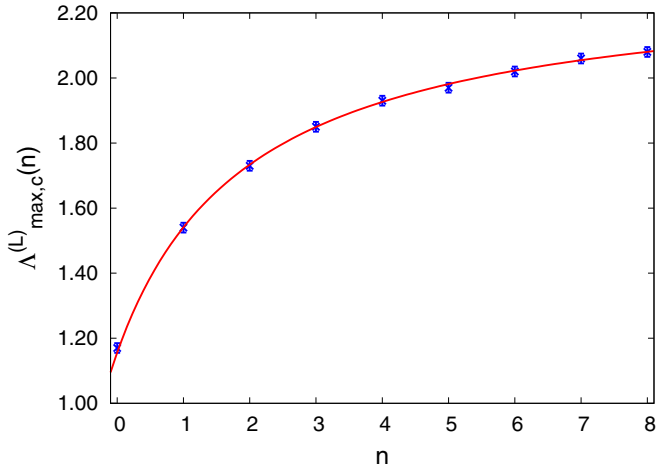

FIG. 11. Position of the critical point for the Haldane-Néel phase transition, for $\Lambda_j \in [\Lambda_{\max}/(n+1), \Lambda_{\max}]$, for all j, where n is an integer number. Here we use $L = 120$ and average over $N_{\rm av} = 40$ realizations of disorder. The value of the critical point $\Lambda^{(L)}_{\max,c}(n)$, for a given n, is estimated as explained for the data in Fig. 7. The red curve corresponds to the fit with the function in Eq. (28).

$\{\Lambda_j\}$ in Eq. (27) equals the critical value Λ_c of the clean chain, i.e., inverting Eq. (27) and showing explicitly the dependence on L:

$$\Lambda^{(L)}_{\max,c}(n) = 2\Lambda^{(L)}_c\,\frac{n+1}{n+2}. \tag{28}$$

As is evident from Fig. 11, the position of the critical point agrees with the scaling given by Eq. (28), where we use $\Lambda^{(L)}_c$ as fit parameter. From the fit, we estimate $\Lambda^{(L)}_c = 1.157 \pm 0.002$, which is not in disagreement with the clean value $\Lambda^{(L)}_c \simeq 1.17$ found in Fig. 7 for $L = 240$. We ascribe the slight discrepancy of the two estimates to finite-size effects (we use $L = 120$ for the data in Fig. 11). Differently from the CIM, the study of the thermodynamic singularities in the case of the XXZ model requires a much larger computational effort, due to the increased numerical complexity. This is left as an open issue for a future work.

V. CONCLUSIONS AND PERSPECTIVES

In conclusion, in this work, we have studied the existence of the nonlocal string order in disordered spin chains. We have focused on two models, the spin-1/2 cluster Ising chain and the spin-1 XXZ Heisenberg chain, which are well known to show a transition from antiferromagnetism to string order in the clean case (the first model is moreover interesting for applications in quantum information [34,35]). We have discovered that this transition persists in both cases if disorder is added.

In the disordered cluster Ising model, we have found a transition from antiferromagnetism to string order by numerically studying the order parameters in the ground state; we did this using the Jordan-Wigner mapping on an integrable free-fermion model. We have seen also that the transition manifests in the fermionic representation as a change in the number of zero-energy edge modes. In this model, we have found analytically the position of the transition point using the strongest coupling renormalization group: this analytical prediction is fully confirmed by the finite-size-scaling on our numerical results. Moreover, studying the thermodynamic singularity at vanishing temperature, we have found a transition between a nonsingular and a singular behavior when the strength of the disorder is increased. We have seen that this transition point is different from the one separating the SO and the AF phase.

In the disordered spin-1 XXZ Heisenberg chain, we have studied the order parameters in the ground state by means of the DMRG technique: we have found a transition between an antiferromagnetic and a string-ordered phase and we have determined its position by means of finite-size scaling. This model is very interesting because its string-ordered phase is adiabatically connected to the celebrated Haldane phase [6] and it can be experimentally studied thanks to the new cold-atom techniques [51].

Perspectives of future work include, first of all, the application of the spin-1 strongest coupling renormalization group [19,29] to the XXZ Heisenberg chain, in order to analytically predict the phase transition point that we find here numerically. Here we have only addressed the properties of the ground state: it will be interesting to consider the properties of the the whole spectrum, in connection with many-body localization (MBL)

[22,23] of an interacting nonintegrable system. MBL systems can show topological order in a large fraction of the excited energy eigenstates [52]: it would be interesting to see if also our nonintegrable spin-1 disordered XXZ model shows MBL and if string and antiferromagnetic order persist in excited states. A possibility to study these phenomena is applying to the Hamiltonian a quantum quench and look at the dynamics of the string correlator. In a clean spin-1 XXZ Heisenberg model, the string thermalizes [53,54], only the ground state being ordered, but in disordered systems the situation could be much different thanks to the MBL.

ACKNOWLEDGMENTS

We are grateful to A. Hamma and L. Mazza for fruitful discussions. We thank E. G. Dalla Torre for useful comments on the manuscript. We acknowledge the CINECA award under the ISCRA initiative, for the availability of high performance computing resources and support. M.C.S. acknowledges partial support from the Israel Science Foundation, Grants No. 231/14 and No. 1452/14. A.R. acknowledges financial support from EU through project QUIC, from "Progetti interni - Scuola Normale Superiore" and from his parents. R.F. kindly acknowledges support from EU through project QUIC (Grant Agreement No. 641122), the National Research Foundation of Singapore (CRP - QSYNC), and the Oxford Martin School.

APPENDIX A: DETAILS ON THE RENORMALIZATION GROUP FOR THE CIM

In the renormalization procedure of the CIM described in Sec. III A, we can distinguish two different types of RG steps: (i) the largest coupling is a J_j or (ii) the largest coupling is a λ_j.

Case (i). If we assume that the largest coupling is J_j, it is not difficult to see that the local Hamiltonian $\hat{H}_0$ of Eq. (11) has four degenerate ground states:

$$\begin{aligned} |1\rangle &= |(+)_{j-1}\uparrow_j(+)_{j+1}\rangle, \\ |2\rangle &= |(-)_{j-1}\uparrow_j(-)_{j+1}\rangle, \\ |3\rangle &= |(-)_{j-1}\downarrow_j(+)_{j+1}\rangle, \\ |4\rangle &= |(+)_{j-1}\downarrow_j(-)_{j+1}\rangle, \end{aligned} \tag{A1}$$

where $|\uparrow_l\rangle, |\downarrow_l\rangle$ are the eigenstates of $\hat{\sigma}_l^z$ and $|(+)_l\rangle, |(-)_l\rangle$ are the eigenstates of $\hat{\sigma}_l^x$.

Applying the degenerate perturbation theory to such four ground states, we get the following corrections at first order in the perturbation $\hat{V}$ of Eq. (12):

$$|\psi_{g1}\rangle = |(+)_{j-1}\uparrow_j(+)_{j+1}\rangle + \frac{i}{2J_j}\left[\lambda_{j-1}\hat{\sigma}^y_{j-2}|(-)_{j-1}\uparrow_j(+)_{j+1}\rangle + \lambda_{j+1}\hat{\sigma}^y_{j+2}|(+)_{j-1}\uparrow_j(-)_{j+1}\rangle\right], \tag{A2}$$

$$|\psi_{g2}\rangle = |(-)_{j-1}\uparrow_j(-)_{j+1}\rangle - \frac{i}{2J_j}\left[\lambda_{j-1}\hat{\sigma}^y_{j-2}|(+)_{j-1}\uparrow_j(-)_{j+1}\rangle + \lambda_{j+1}\hat{\sigma}^y_{j+2}|(-)_{j-1}\uparrow_j(+)_{j+1}\rangle\right], \tag{A3}$$

$$|\psi_{g3}\rangle = |(-)_{j-1}\downarrow_j(+)_{j+1}\rangle - \frac{i}{2J_j}\left[\lambda_{j-1}\hat{\sigma}^y_{j-2}|(+)_{j-1}\uparrow_j(+)_{j+1}\rangle - \lambda_{j+1}\hat{\sigma}^y_{j+2}|(-)_{j-1}\uparrow_j(-)_{j+1}\rangle\right], \tag{A4}$$

$$|\psi_{g4}\rangle = |(+)_{j-1}\downarrow_j(-)_{j+1}\rangle - \frac{i}{2J_j}\left[-\lambda_{j-1}\hat{\sigma}^y_{j-2}|(-)_{j-1}\uparrow_j(-)_{j+1}\rangle + \lambda_{j+1}\hat{\sigma}^y_{j+2}|(+)_{j-1}\uparrow_j(+)_{j+1}\rangle\right]. \tag{A5}$$

In order to apply degenerate perturbation theory, we construct and diagonalize the matrix $V_{ij} = \langle i|\hat{V}|\psi_{gj}\rangle$, which is given by

$$\mathbb{V} = \begin{pmatrix} -\frac{\lambda_{j-1}^2+\lambda_{j+1}^2}{2J_j} & \frac{\lambda_{j-1}\lambda_{j+1}}{J_j}\hat{\sigma}^y_{j-2}\hat{\sigma}^y_{j+2} & 0 & 0 \\ \frac{\lambda_{j-1}\lambda_{j+1}}{J_j}\hat{\sigma}^y_{j-2}\hat{\sigma}^y_{j+2} & -\frac{\lambda_{j-1}^2+\lambda_{j+1}^2}{2J_j} & 0 & 0 \\ 0 & 0 & -\frac{\lambda_{j-1}^2+\lambda_{j+1}^2}{2J_j} & \frac{\lambda_{j-1}\lambda_{j+1}}{J_j}\hat{\sigma}^y_{j-2}\hat{\sigma}^y_{j+2} \\ 0 & 0 & \frac{\lambda_{j-1}\lambda_{j+1}}{J_j}\hat{\sigma}^y_{j-2}\hat{\sigma}^y_{j+2} & -\frac{\lambda_{j-1}^2+\lambda_{j+1}^2}{2J_j} \end{pmatrix}. \tag{A6}$$

This matrix can be written as

$$V_{ij} = \sum_n^{\text{excited states}} \frac{\langle i|\hat{V}|n\rangle\langle n|\hat{V}|j\rangle}{E_{\text{GS}} - E_n}, \tag{A7}$$

where E_{GS} is the energy of the degenerate ground states $|i\rangle$, $|j\rangle$. Diagonalizing this matrix, one finds the perturbed ground-state eigenenergies at second order in λ: $-\frac{\lambda_{j-1}^2+\lambda_{j+1}^2}{2J_j} \pm \frac{\lambda_{j-1}\lambda_{j+1}}{J_j}\hat{\sigma}^y_{j-2}\hat{\sigma}^y_{j+2}$. We select one of these four eigenstates discarding the others. We arbitrarily choose one of the two states with eigenvalue $-\frac{\lambda_{j-1}^2+\lambda_{j+1}^2}{2J_j} - \frac{\lambda_{j-1}\lambda_{j+1}}{J_j}\hat{\sigma}^y_{j-2}\hat{\sigma}^y_{j+2}$. Through the renormalization we have, indeed, eliminated the site j and generated a new coupling

$$-\widetilde{\lambda}_j\hat{\sigma}^y_{j-2}\hat{\sigma}^y_{j+2} \quad \text{with} \quad \widetilde{\lambda}_j \simeq \frac{\lambda_{j-1}\lambda_{j+1}}{J_j}. \tag{A8}$$

These operators $\hat{\sigma}^y_{j-2/j+2}$ are, in principle, different from the unrenormalized ones: they coincide with them up to terms quartic in λ/J.

Case (ii). If the largest coupling is one of the λ_j, we can reduce to the first case by applying to the Hamiltonian (1) the

duality transformation [35]:

$$\hat{\mu}^x_j = \prod_{k=1}^{j} \hat{\sigma}^z_k\,, \quad \hat{\mu}^z_j = \hat{\sigma}^x_j \hat{\sigma}^x_{j+1}. \tag{A9}$$

We find the Hamiltonian in the dual representation as

$$\hat{\tilde{H}} = -\sum_j \left[J_j \hat{\mu}^y_{j-1} \hat{\mu}^y_j + \lambda_j \hat{\mu}^x_{j-1} \hat{\mu}^z_j \hat{\mu}^x_{j+1} \right]. \tag{A10}$$

Indeed, we can see that, in the limit $L \to \infty$ we are considering, this Hamiltonian is equal to its dual in Eq. (1), with λ_j and J_j exchanged. The term with the largest coupling which has to be renormalized is indeed $\hat{\tilde{H}}_0 = -\lambda_j \hat{\mu}^x_{j-1} \hat{\mu}^z_j \hat{\mu}^x_{j+}$. Applying to it the same analysis of the first case, we see that the renormalization procedure eliminates the site j in the dual representation and generates the term in Eq. (15).

It is now easy to show that, after many RG steps, the couplings are renormalized according to

$$\begin{aligned} \widetilde{J}_j &= \frac{J_{j-2l} J_{j-2l+2} \cdots J_{j+2l-2} J_{j+2l}}{\lambda_{j-2l-1} \lambda_{j-2l+1} \cdots \lambda_{j+2l-5} \lambda_{j+2l-3}}\,, \\ \widetilde{\lambda}_j &= \frac{\lambda_{j-2l} \lambda_{j-2l+2} \cdots \lambda_{j+2l-2} \lambda_{j+2l}}{J_{j-2l+1} J_{j-2l+3} \cdots J_{j+2l-3} J_{j+2l-1}}. \end{aligned} \tag{A11}$$

Applying the central limit theorem, we find

$$\begin{aligned} \ln \widetilde{J}_j &= 2l(\overline{\ln J} - \overline{\ln \lambda}) \\ &\quad + \sqrt{2l}(\sqrt{\mathrm{Var}[\ln J] + \mathrm{Var}[\ln \lambda]})u_J\,, \end{aligned} \tag{A12}$$

$$\begin{aligned} \ln \widetilde{\lambda}_j &= 2l(\overline{\ln \lambda} - \overline{\ln J}) \\ &\quad + \sqrt{2l}(\sqrt{\mathrm{Var}[\ln J] + \mathrm{Var}[\ln \lambda]})u_\lambda\,, \end{aligned} \tag{A13}$$

where u_J and u_λ are normally distributed random variables; the averages $\overline{(\ldots)}$ and the variances Var[...] are performed over the distributions of J_j and λ_j. We thus see that, in the limit of infinite RG steps, Eq. (16) holds.

APPENDIX B: DETAILS ON THE NUMERICAL ANALYSIS OF DISORDERED HEISENBERG CHAINS

In this Appendix, we provide details on the strategy that we adopted in order to compute the bulk expectation values of generic two-point observables of the form $\hat{\mathcal{A}}_{k,k+l}$, for the numerical results that have been obtained with the MPS-based algorithm on the spin-1 XXZ Heisenberg chain. We also comment on the analysis of the presence of domain walls in our simulations.

1. Bulk expectation values

To compute the bulk expectation values of $\hat{\mathcal{A}}_{k,k+l}$, we first fix L, $\Lambda_{\min}$, $\Lambda_{\max}$, and a given instance of disorder. For each realization, we numerically compute the space bulk-average by discarding a certain number ΔL of sites that are close to the chain ends. Moreover, we consider distances $l > \Delta L$ such that, provided we are far from the transition point, they are larger than the system's correlation length [50]. Near the critical point, the correlation length tends to diverge, therefore we have always finite-size effects: in order to understand the properties of the transition in the thermodynamic limit, it is thus very important to perform a finite-size scaling as we do in the main text. Specifically, if the sites are labeled from 1 to L, we choose $k = \Delta L = 0.2\,L$ and average the expectation values from $l = l_1 = 0.3\,L$ to $l = l_2 = 0.6\,L$, i.e.,

$$\mathcal{A}_{\mathrm{avg},h} = \frac{1}{l_2 - l_1} \sum_{l=l_1}^{l_2} \langle \hat{\mathcal{A}}_{\Delta L, \Delta L + l} \rangle_h, \tag{B1}$$

where the subscript $_{\mathrm{avg},h}$ denotes the space average for the hth realization of disorder. Then we repeat the simulation by varying the configuration of the disorder in the chain, and perform an average over all the N_{av} realizations:

$$\overline{\mathcal{A}_{\mathrm{avg}}} = \frac{1}{N_{\mathrm{av}}} \sum_{h=1}^{N_{\mathrm{av}}} \mathcal{A}_{\mathrm{avg},h}. \tag{B2}$$

Because of the presence of the random $\{\Lambda_j\}$, the value of $\langle \hat{\mathcal{A}}_{\Delta L, \Delta L + l} \rangle$, as a function of l, is expected to fluctuate in space. Thus the expectation value in Eq. (B1) is affected by an uncertainty, which we estimate via the standard deviation

$$\sigma^2_{\mathcal{A}_h} = \frac{1}{l_2 - l_1} \sum_{l=l_1}^{l_2} (\langle \hat{\mathcal{A}}_{\Delta L, \Delta L + l} \rangle_h - \mathcal{A}_{\mathrm{avg},h})^2. \tag{B3}$$

The fluctuations over the disorder realizations are in turn evaluated via the variance computed from the $\{\mathcal{A}_{\mathrm{avg},h}\}$ in Eq. (B1):

$$\sigma^2_{\bar{\mathcal{A}}} = \frac{1}{N_{\mathrm{av}}} \sum_{h=1}^{N_{\mathrm{av}}} (\mathcal{A}_{\mathrm{avg},h} - \overline{\mathcal{A}_{\mathrm{avg}}})^2. \tag{B4}$$

Finally, to motivate the choice of the spatial averages as in Eq. (B1), we show the behavior of the disorder-averaged string correlator, $\overline{|\mathcal{O}^x_{[1],l}|}$, and the disorder-averaged Néel correlator, $\overline{\mathcal{N}^z_{[1],l}}$, in Fig. 12. Instead of averaging over space for a given realization of disorder, as discussed before, here we average each value of $|\mathcal{O}^x_{[1],l}|(h)$ and of $\mathcal{N}^z_{[1],l}(h)$, for fixed k and l, over N_{av} realization of disorder, where the symbol "(h)" indicates that we are computing the expectation values for the hth realization of disorder [see Eqs. (8) and (26)]. Explicitly,

$$\overline{|\mathcal{O}^x_{[1],l}|} = \frac{1}{N_{\mathrm{av}}} \sum_{h=1}^{N_{\mathrm{av}}} |\mathcal{O}^x_{[1],l}|(h), \tag{B5a}$$

$$\overline{\mathcal{N}^z_{[1],l}} = \frac{1}{N_{\mathrm{av}}} \sum_{h=1}^{N_{\mathrm{av}}} \mathcal{N}^z_{[1],l}(h). \tag{B5b}$$

For the plots in Fig. 12, we choose $k = 0.2L$, $L = 24$, as in Eq. (B1). The red vertical lines limit the interval of l over which we compute the spatial averages in Eq. (B1). We stress that, as for the computation of the bulk expectation values, the two ways of averaging (average over space/disorder and then average over disorder/space) are actually equivalent, but performing the disorder-average for each value of k and l, as in Eqs. (B5), allows us to visualize the average spatial behavior of the string and Néel correlators.

As we see from Fig. 12, apart from spatial fluctuations due to the presence of disorder, the behavior of $\overline{|\mathcal{O}^x_{[1],l}|}$ and

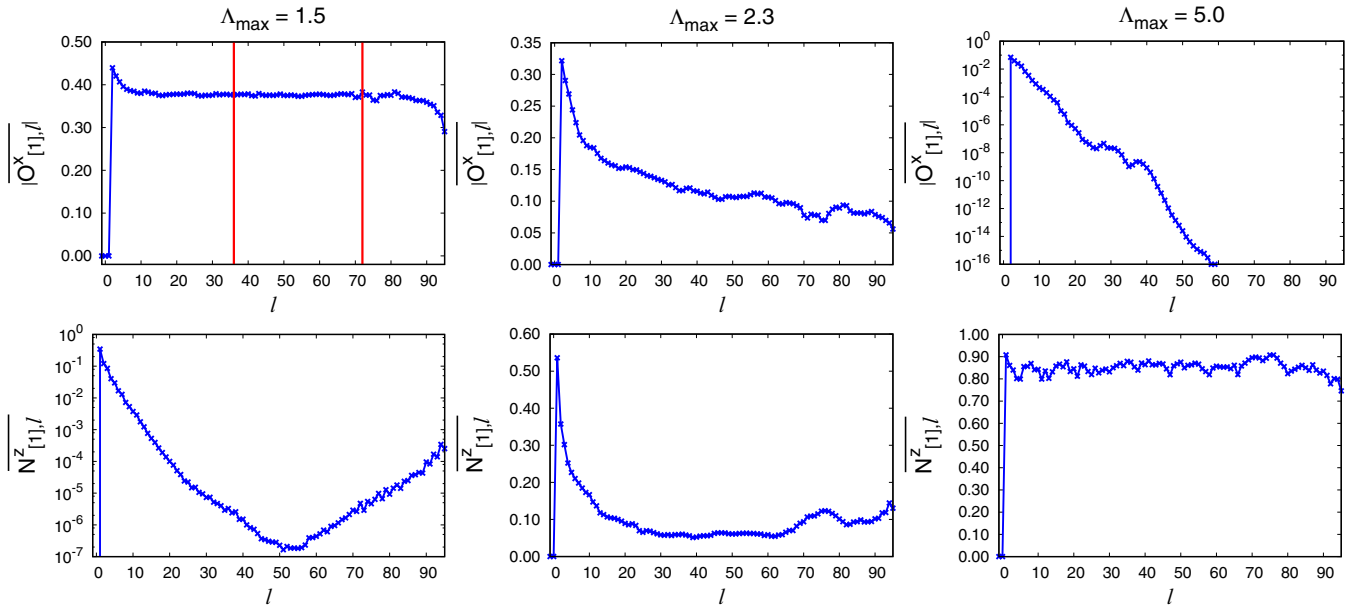

FIG. 12. Disorder-averaged string correlator $\overline{|\mathcal{O}^x_{[1],l}|}$ (top) for $\Lambda_{\max} = 1.5$ (deep Haldane phase, top left), $\Lambda_{\max} = 2.3$ (close to the Haldane-Néel phase transition, top central), and $\Lambda_{\max} = 5.0$ (deep Néel phase, top right), and disorder-averaged Néel correlator $\overline{\mathcal{N}^z_{[1],l}}$ (bottom) for the same values of $\Lambda_{\max}$ as in the top panels. The data refer to the simulation as in Fig. 8. The vertical red lines in the top left panel delimit the domain where we compute the spatial averages. Apart from spatial fluctuations due to the presence of disorder, the behavior of $\overline{|\mathcal{O}^x_{[1],l}|}$ and $\overline{\mathcal{N}^z_{[1],l}}$ is in agreement with the expected behavior in the two phases. The revival of the $\overline{\mathcal{N}^z_{[1],l}}$ correlator in the bottom left panel, for sufficiently large l, is due to finite-size effects.

$\overline{\mathcal{N}^z_{[1],l}}$ is in agreement with the expected behavior in the two phases (see Sec. IV). We also see that the choice of $l_1 = 0.3\,L$ and $l_2 = 0.6\,L$, as in Eq. (B1), allows us to capture the average bulk expectation value, at least sufficiently far away from the transition point. When we are close to the Haldane-Néel phase transition (e.g., Fig. 12, panels with $\Lambda_{\max} = 2.3$), for finite L, our numerical results are affected by finite-size effects, and the correct estimation of the critical point can be then performed only by a finite-size scaling, as explained in Sec. IV.

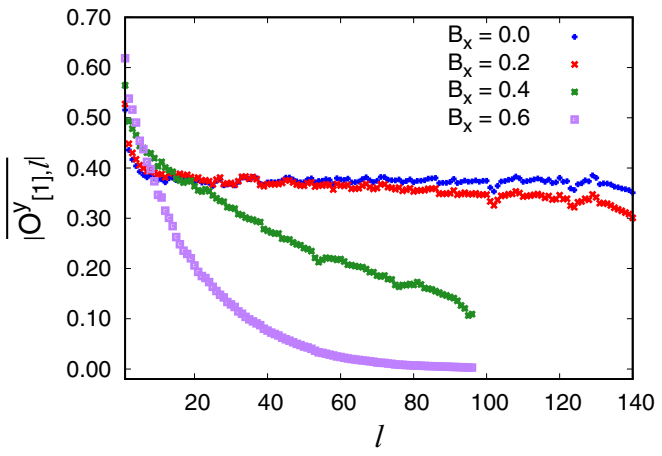

FIG. 13. Numerical results for the string correlator $\overline{|\mathcal{O}^y_{[1],l}|}$ as a function of l computed over the GS of the Hamiltonian in Eq. (B6), for different values of B_x as in the legend, using $L = 180$ (for $B_x = 0,0.2$) and $L = 120$ for the others, and $\Lambda_{\max} = 1.5$. Each point corresponds to the disorder average of $\{|\mathcal{O}^y_{[1],\ell}|(h)\}$, as in Eq. (B5). The addition of $B_x \neq 0$ makes the string correlator decay to zero in the $l \to \infty$ limit.

2. Disordered XXZ model with symmetry-breaking magnetic field

As we mentioned in Sec. II B, we can expect the string-ordered phase to be present in the disordered XXZ model as long as the $\mathbb{D}_2$ symmetry is preserved. We now present some numerical data in order to show an example of destruction of the string order in case a symmetry-breaking term is added to the Hamiltonian. Specifically, we simulate the disordered XXZ model in Eq. (6) with the inclusion of a magnetic field along the x axis:

$$\hat{H}_B = \hat{H}_{\mathrm{XXZ}} + B_x \sum_j \hat{S}^x_j. \tag{B6}$$

Since the $\mathbb{D}_2$ symmetry is broken when $B_x \neq 0$ in Eq. (B6), we expect SO not to be present in the system [32,33]. The result of a simulation with $\Lambda_{\min} = 0$, $\Lambda_{\max} = 1.5$ and different values of B_x (in units of J) is shown in Fig. 13. In order to highlight the different behaviors at long lengths with respect to the $B_x = 0$ case, we use $L = 180$ for $B_x = 0$, 0.2 and $L = 120$ for $B_x = 0.4$, 0.6. We compute the disorder average of the string correlator $\overline{|\mathcal{O}^y_{[1],l}|}$ as in Eq. (B5). As we see, the addition of $B_x \neq 0$ makes the string correlator decay to zero in the $l \to \infty$ limit, and no SO is present in the system, in agreement with the general arguments presented in Refs. [32,33].

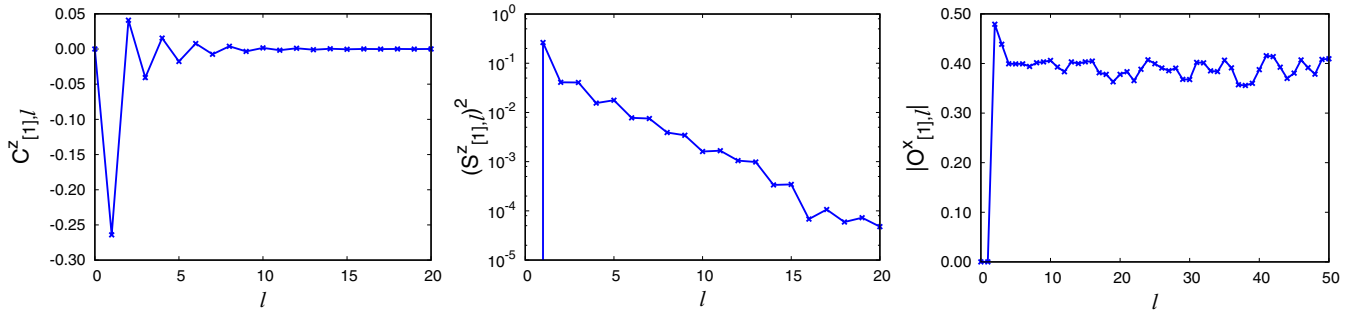

FIG. 14. Typical behavior of the two-point correlator $C^z_{[1],l}$ (left), the staggered correlator $(\mathcal{S}^z_{[1],l})^2$ (central panel), and the string correlator $|\mathcal{O}^x_{[1],l}|$ (right), for a given realization of disorder, in the SO phase at $\Lambda_{\max} = 1.5$. We fix $L = 120$ and $\Lambda_{\min} = 0$. Data are shown for different ranges of l, in order to highlight the salient properties in the three cases. As explained in the text, we fix $k = \Delta L$, with $\Delta L = 0.2\,L$. For $\Lambda_{\max} = 1.5$, the two-point correlator along the z axis oscillates, and it is damped by an exponential decay in the bulk of the chain. This damping is reflected by the exponential decay of the staggered correlator $(\mathcal{S}^z_{[1],l})^2$, whereas the string correlator along the x axis takes a finite value, as expected in the Haldane phase.

3. Domain walls

Let us now consider $\Lambda_{\min} = 0$ and explicitly focus on a case with SO (i) and a case with AF order (ii).

(i) In Fig. 14, we show the results of a simulation with $\Lambda_{\max} = 1.5$ (SO phase) and $L = 120$: two-point correlator $C^z_{[1],l} \equiv \langle \hat{S}^z_k \hat{S}^z_{k+l} \rangle_h$ (left panel), staggered correlator $(\mathcal{S}^z_{[1],l})^2$ (central panel), and string correlator $|\mathcal{O}^x_{[1],l}|$ (right panel). Here, all the correlators have been evaluated over a specific realization of disorder, which we term h. To avoid boundary effects, we choose $\Delta L = 0.2\,L$ (thus, we fix $k = 24$). For this value of $\Delta_{\max}$, we see that $C^z_{[1],l}$ oscillates between positive and negative values, for sufficiently small l, and it is damped by an exponential decay. This is clearly seen in the behavior of $(\mathcal{S}^z_{[1],l})^2$, which exponentially goes to zero in the bulk of the chain. On the other hand, the expectation value of the string operator $\mathcal{O}^x_{[1],l}$ takes a finite value in the bulk of the chain.

(ii) We repeat the same analysis as before, but for $\Lambda_{\max} = 5.0$ (AF phase). The results are shown in Fig. 15. For this value of $\Lambda_{\max}$, the two-point correlator $C^z_{[1],l}$ displays an undamped oscillating pattern, signaling the presence of AF order. However, we notice that the pattern reverses at $l \simeq 29$, i.e., where the data display a kink (domain wall). The presence of such a kink suggests that the AF order appears only locally (the system tends to form domains). In order to see if the presence of domain walls in the pattern of the two-point correlator $C^z_{[1],l}$ is a physical fact or a numerical artifact, we repeat the simulation M times. We fix values of L, $\Lambda_{\min}$, and $\Lambda_{\max}$, and the configuration of disorder $\{\Lambda_j\}$ and in each repetition we vary the initial random MPS state $|\Psi_{\text{in}}\rangle$ at the beginning of the MPS algorithm. Our purpose is to verify that different initial random states produce different configurations of kinks with different GS energies.

To give an example, we show in Fig. 16 the result of several simulations for M different initial random MPS states: $\{|\Psi_{\text{in}}(m)\rangle\}_{m=1,\ldots,M}$. For each value of m, we measure the GS energy, $E_{\text{GS}}(m) = \langle \Psi_{\text{in}}(m)|\hat{H}_{\text{XXZ}}|\Psi_{\text{in}}(m)\rangle$, where $\hat{H}_{\text{XXZ}}$ is the Hamiltonian in Eq. (6), and the number of kinks $N_{\text{kinks}}(m)$, which is obtained from the spatial pattern of $\langle \hat{S}^z_j \rangle$. We define the quantity $\delta E_{\text{GS}}(m) = [E_{\text{GS}}(m) - \min_m\{E_{\text{GS}}(m)\}]/|\min_m\{E_{\text{GS}}(m)\}|$, and compare the values of $\delta E_{\text{GS}}(m)$ with the corresponding number of kinks.

As is evident from Fig. 16, the configurations with zero kinks are associated to the lowest value of the GS energy. Furthermore, we see that the GS energy tends to be larger for

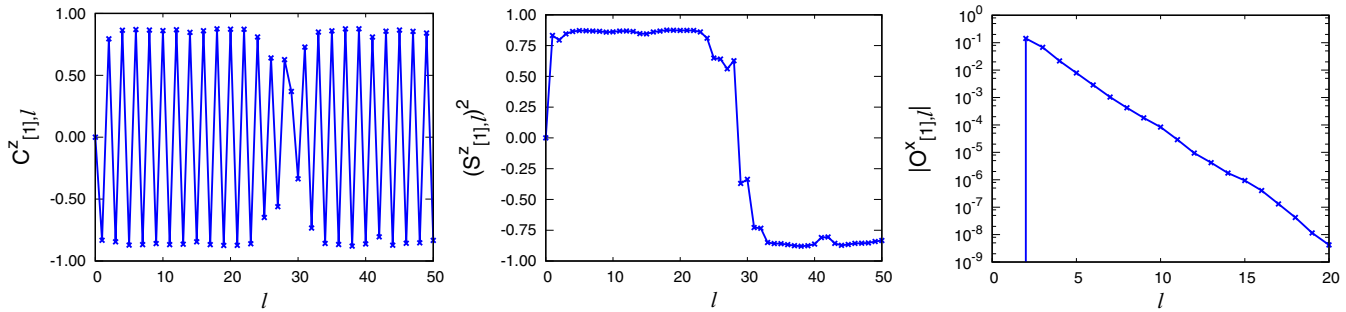

FIG. 15. Same analysis as in Fig. 14, but for the AF phase at $\Lambda_{\max} = 5.0$. In this case, the two-point correlator along the z axis oscillates, signaling the presence of AF order. The presence of a kink at $l \simeq 29$ is expected to be a numerical artifact, due to the nonperfect convergence to the GS of the variational algorithm (see main text and Appendix B). Such a kink is also seen in the staggered correlator, $(\mathcal{S}^z_{[1],l})^2$, as a sign flip in the staggered pattern. The string correlator along the x axis decays exponentially in the bulk, as expected in the Néel phase.

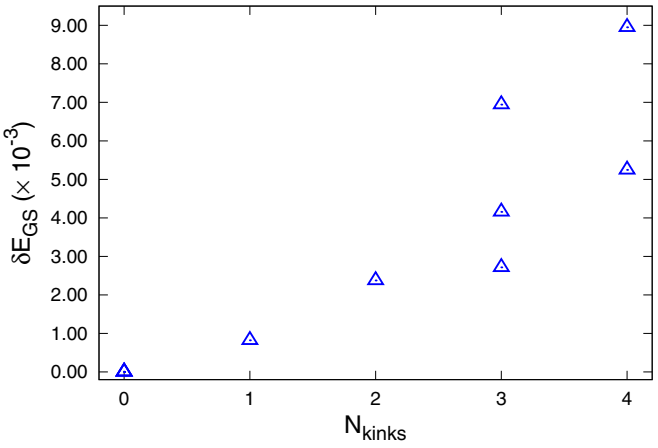

FIG. 16. Values of $\delta E_{\rm GS}$ vs number of kinks $N_{\rm kinks}$. Each point corresponds to a different choice of the random initial MPS state $|\Psi_{\rm in}(m)\rangle$. Simulations are performed for $L = 120$, $\Lambda_{\rm min} = 0$, and $\Lambda_{\rm max} = 5.0$, and taking $M = 10$ initial states.

those configurations having a larger number of kinks. In the present case, we have three configurations with zero kinks (all associated to the same GS energy), one configuration with one and two kinks, three configurations with three kinks, and two configurations with four kinks. Simulations ending up with the same number of kinks may have different GS energy, since the configuration of kinks along the chain varies as well. We see therefore that the number of kinks and their spatial configuration depend on the choice of the initial random MPS state, and that the minimum energy is obtained with zero kinks: We conclude that the presence of domain walls in the magnetization pattern is a numerical artifact. It is due to the fact that the variational MPS algorithm does not perfectly converge to the global minimum of the energy functional.

As a consequence, we expect the true GS to have no kinks: also in the presence of disorder, there is long-range AF order in the Néel phase. This justifies our choice of using the Néel correlator [Eq. (26)] to estimate the staggered correlator $(\mathcal{S}^z_{[1],l})^2$: the Néel correlator does not see the unphysical kinks.

[1] N. Goldenfeld, *Lectures on Phase Transitions and Critical Phenomena* (Avalon Publishing, New York, 1992).
[2] S. Sachdev, *Quantum Phase Transitions*, 2nd ed. (Cambridge University Press, Cambridge, 2011).
[3] B. A. Bernevig and T. Hughes, *Topological Insulators and Topological Superconductors* (Princeton University Press, Princeton, 2013).
[4] A. Altland and B. Simons, *Condensed Matter Field Theory*, 2nd ed. (Cambridge University Press, Cambridge, 2010).
[5] *Topological Phase Transitions and Topological Phases of Matter*, compiled by the Class for Physics of the Royal Swedish Academy of Sciences (2016), available at https://www.nobelprize.org/nobel_prizes/physics/laureates/2016/advanced-physicsprize2016.pdf.
[6] F. D. M. Haldane, Phys. Lett. A **93**, 464 (1983); Phys. Rev. Lett. **50**, 1153 (1983).
[7] W. Chen, K. Hida, and B. C. Sanctuary, Phys. Rev. B **67**, 104401 (2003).
[8] C. D. E. Boschi and F. Ortolani, Eur. Phys. J. B **41**, 503 (2004).
[9] H. Ueda, H. Nakano, and K. Kusakabe, Phys. Rev. B **78**, 224402 (2008).
[10] E. G. D. Torre, E. Berg, and E. Altman, Phys. Rev. Lett. **97**, 260401 (2006).
[11] E. Berg, E. G. D. Torre, T. Giamarchi, and E. Altman, Phys. Rev. B **77**, 245119 (2008).
[12] D. Rossini and R. Fazio, New J. Phys. **14**, 065012 (2012).
[13] T. Kitagawa, E. Berg, M. Rudner, and E. Demler, Phys. Rev. B **82**, 235114 (2010).
[14] B. Friedman, A. Rajak, A. Russomanno, and E. G. D. Torre, arXiv:1708.03400 (2017).
[15] A. Russomanno, B. Friedman, and E. G. D. Torre, Phys. Rev. B **96**, 045422 (2017).
[16] R. B. Griffiths, Phys. Rev. Lett. **23**, 17 (1969).
[17] M. Randeria, J. P. Sethna, and R. G. Palmer, Phys. Rev. Lett. **54**, 1321 (1985).
[18] A. J. Bray, Phys. Rev. Lett. **59**, 586 (1987).
[19] A. Saguia, B. Boechat, and M. A. Continentino, Phys. Rev. Lett. **89**, 117202 (2002).
[20] Y. Dubi, Y. Meir, and Y. Avishai, Nature (London) **449**, 876 (2007).
[21] M. P. A. Fisher, P. B. Weichman, G. Grinstein, and D. S. Fisher, Phys. Rev. B **40**, 546 (1989).
[22] D. M. Basko, I. L. Aleiner, and B. Altshuler, Ann. Phys. **321**, 1126 (2006).
[23] V. Oganesyan and D. A. Huse, Phys.Rev. B **75**, 155111 (2007).
[24] C. Dasgupta and S. K. Ma, Phys. Rev. B **22**, 1305 (1980).
[25] D. S. Fisher, Phys. Rev. B **51**, 6411 (1995).
[26] F. Iglói and C. Monthus, Phys. Rep. **412**, 277 (2005).
[27] R. Mèlin, Y. C. Lin, P. Lajkó, H. Rieger, and F. Iglói, Phys. Rev. B **65**, 104415 (2002).
[28] E. H. Kim, G. Fáth, J. Sólyom, and D. J. Scalapino, Phys. Rev. B **62**, 14965 (2000).
[29] B. Boechat, A. Saguia, and M. A. Continentino, Solid State Commun. **98**, 411 (1996).
[30] P. Lajkó, E. Carlon, H. Rieger, and F. Iglói, Phys. Rev. B **72**, 094205 (2005).
[31] U. Schöllwock, Ann. Phys. **326**, 96 (2011).
[32] F. Pollmann, A. M. Turner, E. Berg, and M. Oshikawa, Phys. Rev. B **81**, 064439 (2010).
[33] D. Pérez-García, M. M. Wolf, M. Sanz, F. Verstraete, and J. I. Cirac, Phys. Rev. Lett. **100**, 167202 (2008).
[34] W. Son, L. Amico, R. Fazio, A. Hamma, S. Pascazio, and V. Vedral, Europhys. Lett. **95**, 50001 (2011).
[35] P. Smacchia, L. Amico, P. Facchi, R. Fazio, G. Florio, S. Pascazio, and V. Vedral, Phys. Rev. A **84**, 022304 (2011).
[36] E. Lieb, T. Schultz, and D. Mattis, Ann. Phys. **16**, 407 (1961).
[37] P. Pfeuty, Ann. Phys. **57**, 79 (1970).
[38] E. Barouch and B. M. Mc Coy, Phys. Rev. A **3**, 786 (1971).
[39] F. Pollmann, E. Berg, A. M. Turner, and M. Oshikawa, Phys. Rev. B **85**, 075125 (2012).
[40] M. den Nijs and K. Rommelse, Phys. Rev. B **40**, 4709 (1989).
[41] T. Kennedy and H. Tasaki, Phys. Rev. B **45**, 304 (1992).
[42] Y. H. Su, S. Y. Cho, B. Li, H.-L. Wang, and H.-Q. Zhou, J. Phys. Soc. Jpn. **81**, 074003 (2012).

[43] A. Russomanno, A. Silva, and G. E. Santoro, J. Stat. Mech. (2013) P09012.

[44] In case of periodic boundary conditions, the Hamiltonian for the clean system can be written as the direct sum of 2×2 blocks, each corresponding to a specific value of the momentum k in the one-dimensional Brillouin zone. The ground state corresponds to a path in the Bloch sphere parameterized by $k \in [0,2\pi]$. The winding number corresponds to the Berry phase [45] accumulated in this path, divided by π. Physically, this number counts how many times the Bloch vector turns around a singularity (a point where the gap of the 2×2 block vanishes), a topological property which cannot be modified by applying continuous transformations. The only way to modify this property is to make the singularity cross the path, which implies breaking the continuity of the path (at the crossing point the gap of the 2×2 Hamiltonian closes and the ground-state Bloch vector is not defined). Therefore, when two phases with different winding number are put into contact, the gap of the Hamiltonian is forced to close at the boundary, that is why the zero-energy boundary modes appear.

[45] M. V. Berry, Proc. R. Soc. London A **392**, 45 (1984).

[46] A. Y. Kitaev, Phys. Usp. **44**, 131 (2001).

[47] J. Alicea, Rep. Prog. Phys. **75**, 076501 (2012).

[48] Y. Niu, S. B. Chung, C.-H. Hsu, I. Mandal, S. Raghu, and S. Chakravarty, Phys. Rev. B **85**, 035110 (2012).

[49] W. DeGottardi, M. Thakurathi, S. Vishveshwara, and D. Sen, Phys. Rev. B **88**, 165111 (2013).

[50] In order to be reliably close to the thermodynamic limit value, one should also ensure that space averages are performed over distances l larger than the typical correlation length of the system. Therefore we perform our averages for $l > \Delta L$ with $\Delta L/L = 0.2$. Near the criticality, the correlation length tends to diverge, therefore finite-size effects are unavoidable. For this reason, the finite-size scaling we perform is so important in order to do statements on the thermodynamic limit behavior.

[51] C. Senko, P. Richerme, J. Smith, A. Lee, I. Cohen, A. Retzker, and C. Monroe, Phys. Rev. X **5**, 021026 (2015).

[52] B. Bauer and C. Nayak, J. Stat. Mech. (2013) P09005.

[53] L. Mazza, D. Rossini, M. Endres, and R. Fazio, Phys. Rev. B **90**, 020301(R) (2014).

[54] M. C. Strinati, L. Mazza, M. Endres, D. Rossini, and R. Fazio, Phys. Rev. B **94**, 024302 (2016).